The Astrophysical Journal, 891:92 (20pp), 2020 March 1 https://doi.org/10.3847/1538-4357/ab6a0d

Wave Excitation by Energetic Ring-distributed Electron Beams in the Solar Corona

Xiaowei Zhou[1,2], Patricio A. Muñoz[3], Jörg Büchner[2,3], and Siming Liu[1]
[1] Key Laboratory of Dark Matter and Space Astronomy, Purple Mountain Observatory, Chinese Academy of Sciences, Nanjing, 210034, People's Republic of China
zhouxw@pmo.ac.cn
[2] Max Planck Institute for Solar System Research, Göttingen, Germany
[3] Center for Astronomy and Astrophysics, Technical University Berlin, Berlin, Germany
Received 2019 July 28; revised 2019 December 31; accepted 2020 January 8; published 2020 March 6

Abstract

We analyzed properties of waves excited by mildly relativistic electron beams propagating along the magnetic field with a ring-shape perpendicular momentum distribution in neutral and current-free solar coronal plasmas. These plasmas are subject to both the beam and the electron cyclotron maser instabilities driven by the positive momentum gradients of the ring-beam electron distribution in the directions parallel and perpendicular to the ambient magnetic field, respectively. To explore the related kinetic processes self-consistently, 2.5D fully kinetic particle-in-cell simulations were carried out. To quantify excited wave properties in different coronal conditions, we investigated the dependences of their energy and polarization on the ring-beam electron density and magnetic field. In general, electrostatic waves dominate the energetics of waves, and nonlinear waves are ubiquitous. In weakly magnetized plasmas, where the electron cyclotron frequency ω_{ce} is lower than the electron plasma frequency ω_{pe}, it is difficult to produce escaping electromagnetic waves with frequency $\omega > \omega_{pe}$ and small refractive index $|ck/\omega| < 1$ (k and c are the wavenumber and the light speed, respectively). Highly polarized and anisotropic escaping electromagnetic waves can, however, be effectively excited in strongly magnetized plasmas with $\omega_{ce}/\omega_{pe} \geqslant 1$. The anisotropies of the energy, circular polarization degree (CPD), and spectrogram of these escaping electromagnetic waves strongly depend on the number density ratio of the ring-beam electrons to the background electrons. In particular, their CPDs can vary from left-handed to right-handed with the decrease of the ring-beam density, which may explain some observed properties of solar radio bursts (e.g., radio spikes) from the solar corona.

Unified Astronomy Thesaurus concepts: Solar magnetic reconnection (1504); Solar corona (1483); Solar coronal radio emission (1993)

1. Introduction

The solar corona consists of a very dynamic, hot and dilute magnetized plasma in which eruptive energy and mass releases take place, such as solar flares and coronal mass ejections. In the course of these solar activity, energetic particles can be accelerated by magnetic reconnection (Zhou et al. 2015, 2016; Muñoz & Büchner 2016, 2018a), shocks (Aschwanden 2002; Benz 2008; Chen et al. 2015), and turbulence (Petrosian & Liu 2004; Fletcher & Hudson 2008; Vlahos & Cargill 2009). These energetic particles can produce electromagnetic emissions from radio to γ-ray wavelengths. Of particular interest are solar radio bursts (SRBs) characterized by (a) high brightness temperatures; (b) short, eruptive timescales; (c) narrow frequency bands; and (d) strong polarization. These characteristics indicate that the SRBs are likely due to coherent emissions of plasma waves caused by plasma instabilities in the solar corona plasma (Melrose 2017). Therefore, SRBs carry rich information of plasma dynamics in the solar corona and may be used to remotely study the related plasma processes.

SRBs can be classified into many types by their distinctive structures in the dynamical spectrum (or spectrogram; Wild et al. 1963). Among all types of the SRBs, spikes immediately attracted the attention of researchers since their first detections (Droege & Riemann 1961; Elgarøy 1961; De Groot 1962) owing to their particular observed properties: extremely short duration (down to and probably even less than a few milliseconds, limited by the time resolution of radio telescopes), narrow bandwidth (<1%), and mostly X-mode-dominated high degree of polarization (can be ≈100%; see, e.g., Fleishman & Mel'nikov 1998 for a review and references therein). Solar radio spikes are closely related to particle acceleration and primary energy release processes in solar flares. They might provide direct information on the finest structure of these energy release processes (Benz 1985, 1994). To deduce energy release information of solar flares from observations of solar radio spikes, one first needs a reliable generation mechanism for these solar radio spikes. Since right-handed polarized X-mode waves are predominant in most cases of solar radio spikes, electron cyclotron maser (ECM) emission (Twiss 1958; Gaponov 1959; Schneider 1959) has been widely accepted as the most likely coherent emission mechanism for their generation (Dulk 1985; Vlahos 1987; Vlahos & Sprangle 1987; Melrose 1994; Fleishman & Mel'nikov 1998).

The so-called ECM mechanism, proposed by Twiss (1958), is a consequence of a linear ECM instability, where electromagnetic waves absorb the energy of energetic electrons, i.e., negative absorption of waves by energetic electrons, via wave–particle interactions (see Melrose 2017, chap. 3.2). Besides solar radio spikes, the ECM mechanism was also applied to the generation of Earth's auroral kilometric radiation (AKR; Wu & Lee 1979; Lee & Wu 1980; Lee et al. 1980; Strangeway et al. 2001) and Jupiter's decametric emission (DAM; Goldreich & Julian 1969). For the ECM mechanism to operate on remote radio emissions, first the electron cyclotron frequency ω_{ce} needs to be greater than the plasma frequency ω_{pe} in the generation sites of radio emissions, since strong wave excitations by the ECM instability are mainly located around ω_{ce} and waves with

frequencies below local ω_{pe} cannot escape from a plasma directly, i.e., the escape condition (e.g., Melrose 2017). The condition $\omega_{ce} > \omega_{pe}$, however, implies high local Alfvén velocities $\sim 0.02c$ (Wu et al. 2014), which cannot be easily satisfied within the standard model of the solar atmosphere (Wild 1985; Wu 2012, 2014; Wu et al. 2014). Wu et al. (2014) and Chen et al. (2017) suggested that the condition $\omega_{ce} > \omega_{pe}$ can be fulfilled if local density cavities form, e.g., due to fluctuations in the ubiquitous Alfvénic turbulence. Such density cavities are, indeed, found recently along the path of the electron beam propagating parallel to the low-density separatrices of strong-guide-field magnetic reconnection via 3D fully kinetic particle-in-cell (PIC) simulations (Drake et al. 2003; Pritchett & Coroniti 2004; Muñoz & Büchner 2018b). Observations by Régnier (2015) and Morosan et al. (2016) also demonstrated that the condition of $\omega_{ce} > \omega_{pe}$ can be satisfied within some areas of the solar corona, such as the core of a large active region.

Furthermore, to trigger the ECM emission (i.e., the ECM instability), a positive gradient is required in the electron momentum distribution perpendicular to the ambient magnetic field, i.e., $\partial f/\partial u_\perp > 0$, where f is the electron momentum distribution and $u_\perp$ is the perpendicular momentum of electrons. This property, called population inversion, drives the maser instability. Possible momentum distributions with $\partial f/\partial u_\perp > 0$ include ring distributions (Pritchett 1984; Vandas & Hellinger 2015), loss-cone distributions (Wu & Lee 1979; Tsang 1984), and horseshoe distributions (Pritchett et al. 1999; Melrose & Wheatland 2016).

$\partial f/\partial u_\perp > 0$ was obtained by considering particle acceleration in the outflow region of magnetic reconnection, where cup-like momentum distributions are found (Büchner & Kuska 1996). Energetic particles' magnetic gradient drifts can also cause a redistribution of the energy of parallel-flowing beam particles to the perpendicular direction (Zhou et al. 2015), forming ring or crescent-shaped momentum distributions in the perpendicular direction (Voitcu & Echim 2012, 2018). Vlahos & Sprangle (1987) and Vlahos (1987) mentioned that the interaction of quasi-perpendicular shocks with the ambient solar coronal plasma might lead to formation of a ring momentum distribution in the direction perpendicular to the ambient magnetic field. A quasi-perpendicular shock-related SRB event during a solar flare was reported by Chen et al. (2015). Additionally, by means of fully kinetic PIC simulations, it has been proved that ring momentum distribution in the direction perpendicular to the ambient magnetic field can indeed be produced during magnetic reconnection (Bessho et al. 2014; Shuster et al. 2014, 2015). Moreover, electron holes in the electron exhaust regions at the X-points of magnetic reconnection could also provide $\partial f/\partial u_\perp > 0$ for the ECM emissions (Treumann et al. 2011, 2012; Treumann & Baumjohann 2017). Note that gradients in the parallel direction $\partial f/\partial u_\parallel$ can also drive ECM emissions. This requires, however, extremely anisotropic electron momentum distributions, e.g., $(\Delta u_\perp/c)^2 \geqslant \Delta u_\parallel/c$ for a bi-Maxwellian electron momentum distribution, where $\Delta u_\perp$, $\Delta u_\parallel$, and c are the perpendicular and parallel thermal momenta of electrons and the speed of light, respectively (Melrose 1973, 2017). There is, however, no observational evidence for the existence of such strong anisotropy in the solar corona.

On the other hand, energetic electrons always follow a beam momentum distribution in the direction along the coronal magnetic field based on some high-energy phenomena in the solar corona, e.g., type III SRBs, hard X-ray bursts, and solar energetic particle events (Cairns et al. 2018; Chen et al. 2015, 2018). 3D fully kinetic PIC and test particle simulations have also shown that strongly energized electron beams can be generated by guide-field magnetic reconnection (Büchner et al. 2018; Muñoz & Büchner 2018a; Zhou et al. 2016). The beam momentum distribution is unstable to the beam instability driven by free energies from electrons with a momentum distribution f containing $u_\parallel \cdot \partial f/\partial u_\parallel > 0$ (see Melrose 1986; Gary 1993). The classical theory of plasma emission, suggested by Ginzburg & Zhelezniakov (1958), is based on this beam instability.

The plasma emission mechanism contains nonlinear three-wave interaction processes. The theory starts with the excitation of electrostatic Langmuir waves (L) via the beam instability. Then, backward-directed Langmuir (L') waves can be generated via the electrostatic decay or induced backscattering of forward-directed Langmuir waves by fluctuations of ions ($L \rightarrow L' \pm S$, where S represents ion-acoustic wave; see Umeda 2010). Electromagnetic decay or coalescence of L and S waves will lead to the fundamental electromagnetic emission ($T_{\omega_{pe}}$) at the electron plasma frequency ω_{pe} ($L \rightarrow T_{\omega_{pe}} \pm S$), while the second harmonic electromagnetic emission ($T_{2\omega_{pe}}$) at $2\omega_{pe}$ can be produced by the coupling of L and L' waves ($L + L' \rightarrow T_{2\omega_{pe}}$; Karlický & Bárta 2011; Melrose 2017; Henri et al. 2019). Generally, the classical plasma emission processes will lead to excitations of the L, L', $T_{\omega_{pe}}$, $T_{2\omega_{pe}}$, and S waves owing to the beam instability. Recently, Umeda (2010) proposed an alternative mechanism for the generation of the L' waves with two symmetric counter-propagating electrons beams, where the L and L' waves can be directly induced by the forward- and backward-propagating electron beams, respectively (Ganse et al. 2012a, 2012b; Thurgood & Tsiklauri 2015). The plasma emission theory has been widely used to explain the formations of type I, II, and III SRBs (Aschwanden 2005; Melrose 2017). In situ spacecraft observations of the interplanetary type III SRBs have also confirmed the plasma emission theory (Lin et al. 1981; Ergun et al. 1998). By considering many propagation effects (e.g., wave scattering, decreasing magnetic field strength, interplanetary shocks) during the transportation of energetic electrons from the solar corona to the interplanetary medium (IPM), momentum distributions of the energetic electrons in the solar corona should be quite different from those in the IPM.

Both the beam and ECM instabilities (driven by free energies in $u_\parallel \cdot \partial f/\partial u_\parallel > 0$ and $\partial f/\partial u_\perp > 0$ distributions, respectively) have been invoked separately to explain the coherent emission mechanism of different types of SRBs (see, e.g., Aschwanden 2005; Melrose 2017, for reviews of SRBs). For a more general application to the microscopic emission processes in plasmas, here we will generalize these two distributions and characterize the properties of emission processes due to both instabilities. On the other hand, based on the above-mentioned theoretical studies and numerical simulations, both free energies with population inversion $u_\parallel \cdot \partial f/\partial u_\parallel > 0$ and $\partial f/\partial u_\perp > 0$ in the electron momentum distribution and density cavity with $\omega_{ce} > \omega_{pe}$ can be realized simultaneously in the dynamically evolving fast solar magnetic reconnection events in the solar corona.

In this paper, via 2.5D fully kinetic PIC simulations, we investigate properties of waves excited by mildly relativistic ring-beam electrons in neutral and current-free solar coronal plasmas. In this system, the ring-beam electrons, together with

protons and background electrons, support the global charge and current neutralities, respectively. Many theories and observations have proved that the majority of the current induced by energetic beam electrons can be rapidly compensated by the return current of drifting background electrons (e.g., Brown & Bingham 1984; van den Oord 1990; Melrose 1990; Khodachenko et al. 2009). Note that nonzero net current in plasmas can not only introduce a current instability (see Melrose 1986; Matsumoto & Omura 1993; Wu et al. 2014; Chen et al. 2017) but also generate strong magnetic fields and oscillations, leading to a very complex plasma system (Henri et al. 2019).

Some parametric dependence of the wave excitations resulting from the electron ring-beam momentum distribution has been investigated by Lee et al. (2011) utilizing 2.5D fully kinetic PIC simulations. In particular, these authors explored the influences of the average kinetic energy and pitch angle of the ring-beam electrons on the wave excitations, keeping the density ratio of ring-beam and background electrons fixed ($n_{\rm rb}/n_{\rm bg}$ =1:19), as well as the frequency ratio $\omega_{\rm ce}/\omega_{\rm pe} = 5$. In order to derive properties of waves generated by energetic ring-beam electrons at different locations along the beam trajectory in the solar corona, we utilize a 2.5D version of the fully kinetic PIC code ACRONYM to explore the dependences of the nonlinear wave generation and saturation by energetic ring-beam electrons on the frequency ratio of $\omega_{\rm ce}/\omega_{\rm pe}$ and the density ratio of the ring-beam $n_{\rm rb}$ to background $n_{\rm bg}$ electrons with the average kinetic energy and pitch angle of the ring-beam electrons fixed.

Compared with previous studies (e.g., Pritchett 1984; Lee et al. 2009, 2011), we have developed precise diagnostics to investigate the nonlinear evolution, saturation, and anisotropy of different electromagnetic wave modes guided by the dispersion relations of a magnetized cold plasma (see Section 2.2.1). Since only electromagnetic waves with frequency $\omega > \omega_{\rm pe}$ and small refractive index $|ck/\omega| < 1$ can escape from their generation sites and might be detected by remote detectors, polarization, spectrogram, and anisotropies of these escaping electromagnetic waves are explored to compare with the ground-based observations of solar radio spikes (see Section 2.2.2).

This paper is organized as follows: after the introduction, we present the numerical simulation model in Section 2. Section 3 contains the key results of this study, and in Section 4 we draw our conclusions and discuss the application of our results.

2. Numerical Simulation

2.1. Model and Setup

Since the excitation and growth of waves driven by plasma instabilities are, in general, kinetic and nonlinear processes, self-consistent kinetic simulations are required to investigate them. In these simulations, particle interactions through the electromagnetic fields and effects of particles' motions on the electromagnetic fields, as well as nonlinear wave–wave and wave–particle interactions, can be correctly incorporated. Our tool of choice is a fully kinetic PIC code, which can model all those processes from a first-principle approach. In a fully kinetic PIC code, generally, the electromagnetic fields are calculated from the Maxwell equations with the charge and current densities by knowing the positions and velocities of all particles. And then the particles move owing to these electromagnetic fields from the Newton–Lorentz equation of motion, and the new positions and velocities of particles lead to a new state of the electromagnetic fields. This step is equivalent to solving the effective Vlasov equation for the (numerical) particles. These steps are repeated until the end of a simulation. Therefore, the fully kinetic PIC algorithm solves the full set of the Vlasov–Maxwell equations (see, e.g., Birdsall & Langdon 1991; Tskhakaya et al. 2007; Lapenta 2012; Vay & Godfrey 2014, for reviews of the basic theories and applications of fully kinetic PIC codes).

We performed this study with the fully kinetic PIC code—ACRONYM (http://plasma.nerd2nerd.org/; Kilian et al. 2017), a fully relativistic electromagnetic code tuned for the study of kinetic-scale plasma wave phenomena and interactions in collisionless plasmas in a wide variety of physical environments (see, e.g., Ganse et al. 2012a; Kempf et al. 2016; Muñoz & Büchner 2016, 2018b; Schreiner et al. 2017; Büchner et al. 2018). We use its version in two spatial dimensions and three dimensions in momentum and components of the electromagnetic fields (i.e., 2.5D).

The 2D simulation box contains 1024 × 1024 grid points in the x–y plane. Periodic boundaries are applied in both directions for both fields and particles. In our simulations, to keep the global charge neutrality, three species of particles are employed, one for the mildly relativistic ring-beam electrons and the other two species for the protons and the background electrons. For physically realistic results, the proton-to-electron mass ratio has been chosen as the physical $m_p/m_e = 1836$. Initially, 2000 particles per cell are implemented to reduce the numerical noise (Hockney 1971; Dawson 1983; Birdsall & Langdon 1991). These particles are homogeneously distributed in the whole simulation domain with a constant ambient magnetic field $\boldsymbol{B}_0 = B_0\boldsymbol{x}$ along the x-axis, since typical domain sizes modeled by fully kinetic PIC simulations are much smaller than the typical length scale of the density and magnetic field gradients in the solar corona.

The initial momentum distributions of all particles (both electrons and protons) are characterized in terms of momentum per unit mass, $\boldsymbol{u} = \gamma\boldsymbol{v}$, where $\gamma = 1/\sqrt{1 - v^2/c^2} = \sqrt{1 + u^2/c^2}$. Note that, hereafter, we will simply refer to "momentum per unit mass" as "momentum." Correspondingly, the momentum distribution for the mildly relativistic ring-beam electrons is (Umeda et al. 2007; Lee et al. 2011; Kainer & MacDowall 1996)

$$
\begin{aligned}
F_{\rm rb}(u_\parallel, u_\perp) &= F_{\rm rb\parallel}(u_\parallel)F_{\rm rb\perp}(u_\perp)\\
F_{\rm rb\parallel}(u_\parallel) &= \frac{1}{\sqrt{2\pi}\,u_{\rm th\parallel}}\exp\left[-\frac{(u_\parallel - u_{\rm rb\parallel})^2}{2u_{\rm th\parallel}^2}\right]\\
F_{\rm rb\perp}(u_\perp) &= \frac{1}{2\pi u_{\rm th\perp}^2 Q_\perp}\exp\left[-\frac{(u_\perp - u_{\rm rb\perp})^2}{2u_{\rm th\perp}^2}\right],
\end{aligned}
\tag{1}
$$

where $u_\parallel$, $u_\perp$ are the particle momenta along and perpendicular to the ambient magnetic field $\boldsymbol{B}_0$, respectively. ($u_{\rm rb\parallel}$, $u_{\rm rb\perp}$) and ($u_{\rm th\parallel}$, $u_{\rm th\perp}$) are their corresponding bulk drift and thermal momenta ($v_{\rm th\parallel} = u_{\rm th\parallel}/\gamma_{\rm th} = \sqrt{k_{\rm B}T_{e,\parallel}/m_e}$ and $v_{\rm th\perp} = u_{\rm th\perp}/\gamma_{\rm th} = \sqrt{k_{\rm B}T_{e,\perp}/m_e}$, where $T_{e,\parallel}$ ($T_{e,\perp}$) is the parallel (perpendicular) electron temperature, $k_{\rm B}$ is Boltzmann's constant, and $\gamma_{\rm th} = \sqrt{1 + (u_{\rm th\parallel}^2 + u_{\rm th\perp}^2)/c^2}$). According to our simulations, the parallel and perpendicular directions are along the x-axis

and y-axis, respectively. Considering the typical velocity of energetic beam electrons (Wild et al. 1959; Alvarez & Haddock 1973; Suzuki & Dulk 1985; Reid & Ratcliffe 2014) and typical temperature in the solar corona, initially we take $\gamma = \sqrt{1 + (u_{\rm rb\parallel}^2 + u_{\rm rb\perp}^2)/c^2} = 1.2$ ($\sim$100 keV and $\sqrt{u_{\rm rb\parallel}^2 + u_{\rm rb\perp}^2} = 0.67c$) as the average initial kinetic energy of the ring-beam electrons. Their averaged pitch angle is $\phi_0 = \tan^{-1}(u_{\rm rb\perp}/u_{\rm rb\parallel}) = 30°$, which indicates that the ring-beam electrons have more energies in the $\boldsymbol{B}_0$ parallel direction. And $u_{\rm th\parallel} = u_{\rm th\perp} = u_{\rm rbth} = u_{\rm th} = 0.025c$. $Q_\perp$ in Equation (1) is the normalization constant

$$Q_\perp = \exp\left[-\frac{u_{\rm rb\perp}^2}{2u_{\rm th\perp}^2}\right] + \sqrt{\frac{\pi}{2}}\frac{u_{\rm rb\perp}}{u_{\rm th\perp}}\,{\rm erfc}\left[-\frac{u_{\rm rb\perp}}{\sqrt{2}\,u_{\rm th\perp}}\right]. \quad (2)$$

For a current-free system, all the background electrons drift in the opposite direction to that of the ring-beam electrons with a momentum $u_{\rm bg\parallel} = -u_{\rm rb\parallel}n_{\rm rb}/n_{\rm bg}$, where $n_{\rm rb}$ and $n_{\rm bg}$ are the number densities of the ring-beam and background electrons, respectively (Karlický & Bárta 2009; Ganse et al. 2012b).

The background electrons, hence, follow a drifting Maxwellian momentum distribution with a thermal spread $u_{\rm bgth} = 0.05c$ along each dimension. The backward-drifting background electrons, hence, also contain free energies $u_\parallel \cdot \partial f/\partial u_\parallel > 0$ for the beam instability. Protons are used for the global charge neutrality. They are assumed to follow an isotropic Maxwellian momentum distribution with the same temperature as the background electrons. Note that protons are quite important for the generation of the ion-acoustic waves in the plasma emission mechanism, so that we let them move freely, i.e., our simulations also solve the equations of motion for the protons, even though they respond to electromagnetic forces at much larger timescales than electrons.

Due to the free energies provided by the ring-beam and backward-drifting background electrons, both the beam and ECM instabilities can be driven owing to the positive gradients $u_\parallel \cdot \partial f/\partial u_\parallel > 0$ and $\partial f/\partial u_\perp > 0$ in the electron momentum distribution, respectively. To distinguish contributions from the beam and ECM instabilities, we also carry out simulations with only either a pure-beam or a pure-ring momentum distribution for the energetic electrons ($u_{\rm rb\perp} = 0$ or $u_{\rm rb\parallel} = 0$, respectively), while other parameters are the same as these ring-beam simulations.

In this study, all quantities are solved in real (spatial-temporal) space with CGS units, and all simulations have the same spatial and time resolution. In particular, the grid cell size is $\Delta x = \Delta y \simeq \lambda_{\rm De}$, where $\lambda_{\rm De} = u_{\rm th}/\omega_{\rm pe}$ is the electron Debye length and $\omega_{\rm pe}$ is the total electron plasma frequency, i.e., $\omega_{\rm pe} = \sqrt{\omega_{\rm prb}^2 + \omega_{\rm pbg}^2} = \sqrt{4\pi n_t e^2/m_e}$, where $n_t = n_{\rm rb} + n_{\rm bg}$ and e are the total number density and charge of electrons, respectively. And $\omega_{\rm prb}$ ($\omega_{\rm pbg}$) is the plasma frequency of the ring-beam (background) electrons. The time step in our simulations is determined by the inherent length and timescale requirements in a fully kinetic PIC code, i.e., the Courant–Friedrichs–Lewy (CFL) condition for the speed of light c. Correspondingly, our simulations can cover $|k_{x,y}/(\omega_{\rm pe}/c)| < 92.2$ and $|\omega/\omega_{\rm pe}| < 12.3$ with resolutions $\Delta k_{x,y} = 0.18\omega_{\rm pe}/c$ and $\Delta\omega = 0.015\omega_{\rm pe}$, respectively, in the wavevector–frequency ($\boldsymbol{k} - \omega$) space.

Variable parameters are $n_{\rm rb}/n_t$ (being equal to 5%, 10%, 20%, 30%, 40%, 50% with fixed $\omega_{\rm ce}/\omega_{\rm pe} = 5$; see Section 3.1) and $\omega_{\rm ce}/\omega_{\rm pe}$ (being equal to 0.2, 0.3, 0.5, 1, 2, 3 with fixed $n_{\rm rb}/n_t = 5\%$; see Section 3.2). Note that simulation with $n_{\rm rb}/n_t = 5\%$ and $\omega_{\rm ce}/\omega_{\rm pe} = 5$ can be compared with Case B in the study of Lee et al. (2011). The ambient magnetic field $\boldsymbol{B}_0$ is initialized based on the frequency ratio $\omega_{\rm ce}/\omega_{\rm pe}$. Note that the values of the ratio of beam to total density are probably much higher than those thought to exist in the solar corona, but they could be considered appropriate for density cavities, where the background density drops considerably. In addition, fully kinetic PIC simulations of magnetic reconnection tend to generate electron beams, propagating through the low-density separatrices, with similar density ratios (Muñoz & Büchner 2016).

Normalizations used throughout this paper are as follows: $\omega_{\rm norm} = 5.0\omega_{\rm pe}$ is the normalization of frequency. Time, momentum, and distance are normalized by $1/\omega_{\rm norm}$, c, and $c/\omega_{\rm norm}$, respectively. $B_{\rm norm}$ is the normalization of the electric and magnetic field strengths and corresponds to the ambient magnetic field $\boldsymbol{B}_0$ for $\omega_{\rm ce}/\omega_{\rm pe} = 5.0$. Energy is normalized by the magnetic field energy $\varepsilon_{\rm norm}$ corresponding to a uniform $B_{\rm norm}$ in the whole simulation domain.

2.2. Diagnostic Method

2.2.1. Energy in Wave Modes

Since all quantities in our simulations are given in real (spatial-temporal) space, to characterize the plasma waves, one applies fast Fourier transforms (FFTs) on the electromagnetic fields over the spacetime domain of the simulations. Meanwhile, different wave modes are distinguished by their own dispersion relation. To estimate the energy contained by different wave modes, we should consider their dispersion relations. As a simplification, we take the wave dispersion relations in the magnetized cold plasma as an approximation (see, e.g., Andre 1985; Melrose 1986; Stix 1992), despite that the criteria for the validity of the cold-plasma approximation (Melrose 1986; Stupp 2000) could not be always satisfied in our simulations. For a numerical simulation, different from theoretical studies, these criteria are, however, difficult to adopt since the effective electron temperatures in simulated plasmas are quite inhomogeneous and dynamic. Generally, the cold-plasma dispersion relation constitutes a good approximation to the full hot plasma dispersion relation in many conditions (Chen et al. 2013).

We also assume that energy spectral density of a wave mode M, i.e., $I_M(\boldsymbol{k}, \omega)$, follows a Gaussian frequency distribution around its dispersion surface in the $\boldsymbol{k} - \omega$ space (Comişel et al. 2013):

$$I_M(\boldsymbol{k}, \omega) = \sum_m |A_{m,M}(\boldsymbol{k}, \omega)|^2 \quad (3)$$

$$A_{m,M}(\boldsymbol{k}, \omega) = A_m(\boldsymbol{k}, \omega) \cdot \left\{\frac{1}{\sqrt{2\pi}\,\sigma}\exp\left[-\frac{(\omega - \omega_{M\rm cold}(\boldsymbol{k}))^2}{2\sigma^2}\right]\right\}^{1/2}, \quad (4)$$

where $\omega_{M\rm cold}(\boldsymbol{k})$ denote the frequency of the wave mode M at the given wavevector $\boldsymbol{k}$ (dispersion relation) in the magnetized cold-plasma approximation. σ characterizes the frequency broadening for the wave mode M around its corresponding cold-plasma dispersion relation surface. Here we use $\sigma = 0.05\omega_{\rm norm}$ for each

wave mode as a simplification. And m indicates different components of the electromagnetic fields ($\vec{\mathbf{E}}$, $\vec{\mathbf{B}}$). We apply FFTs on the electromagnetic field components $a_m(x, y, t)$ over the entire space and time domain of our simulations to get their fluctuations $A_m(\boldsymbol{k}, \omega) = \mathrm{FFT}_{x,y,t}[a_m(x, y, t)]$ in $\boldsymbol{k} - \omega$ space. And then a Gaussian filter is applied on $A_m(\boldsymbol{k}, \omega)$ to get the electromagnetic field component fluctuations of the wave mode M, i.e., $A_{m,M}(\boldsymbol{k}, \omega)$. This method is hereinafter called the Gaussian filter method.

For the (temporal) evolution of energy of the wave mode M, an inverse FFT (IFFT) is implemented on $A_{m,M}(\boldsymbol{k}, \omega)$ (Equation (4)) in the frequency ω space. An integration over the wavevector $\boldsymbol{k}$ space is applied on the IFFT results to get the energy evolution of the electromagnetic field component m, i.e.,

$$\varepsilon_M(t) = \sum_m \sum_{\boldsymbol{k}} |\mathrm{IFFT}_\omega[A_{m,M}(\boldsymbol{k}, \omega)]|^2 \Delta\boldsymbol{k}. \tag{5}$$

For the study of the wave energy along different wave propagation directions, we integrate $I_M(\boldsymbol{k}, \omega)$ in the $\boldsymbol{k} - \omega$ space only if $\cos\theta = k_\parallel/k$ is satisfied, where θ is the pitch angle between the $\boldsymbol{k}$ and $\boldsymbol{B}_0$ and $k_\parallel$ is the $\boldsymbol{B}_0$ parallel component of the wavevector $\boldsymbol{k}$, and then the energy of the wave mode M along the direction θ is

$$\varepsilon_M(\theta) = \sum_\omega \sum_{\boldsymbol{k}} I_M(\boldsymbol{k}, \omega)\delta(k_\parallel/k - \cos\theta)\Delta\boldsymbol{k}\Delta\omega, \tag{6}$$

where $\delta(*)$ is the Dirac delta function.

2.2.2. Polarization

To get the polarization of waves propagating along each direction, the polarization vector $\boldsymbol{e}_p$ is defined with respect to the wave propagation vector $\boldsymbol{k}$ in the x–y plane (Melrose 1986; Willes & Cairns 2000; Bittencourt 2004):

$$\boldsymbol{e}_p = \begin{pmatrix} \boldsymbol{e}_1 = \boldsymbol{k}/|k| \\ \boldsymbol{e}_2 = \boldsymbol{e}_3 \times \boldsymbol{e}_1 \\ \boldsymbol{e}_3 = \boldsymbol{e}_z \end{pmatrix}, \tag{7}$$

where $\boldsymbol{e}_z = \boldsymbol{e}_x \times \boldsymbol{e}_y$ is the unit vector in the direction perpendicular to the x–y plane. To separate the left- and right-handed polarized components ($E_l(\boldsymbol{k}, \omega)$, $E_r(\boldsymbol{k}, \omega)$) of the transverse electric fields, i.e., perpendicular components of $\boldsymbol{E}(\boldsymbol{k}, \omega)$ with respect to $\boldsymbol{k}$, a circular basis ($\boldsymbol{e}_l$, $\boldsymbol{e}_r$) is defined based on the polarization vector $\boldsymbol{e}_p$ in Equation (7):

$$\boldsymbol{e}_l = \begin{cases} (\boldsymbol{e}_2 + i\boldsymbol{e}_3)/\sqrt{2} & [\omega \cdot k_\parallel > 0 \quad \text{or} \quad (k_\parallel = 0 \quad \text{and} \quad \omega \cdot k_\perp > 0)] \\ (\boldsymbol{e}_2 - i\boldsymbol{e}_3)/\sqrt{2} & [\omega \cdot k_\parallel < 0 \quad \text{or} \quad (k_\parallel = 0 \quad \text{and} \quad \omega \cdot k_\perp < 0)] \end{cases}$$

$$\boldsymbol{e}_r = \begin{cases} (\boldsymbol{e}_2 - i\boldsymbol{e}_3)/\sqrt{2} & [\omega \cdot k_\parallel > 0 \quad \text{or} \quad (k_\parallel = 0 \quad \text{and} \quad \omega \cdot k_\perp > 0)] \\ (\boldsymbol{e}_2 + i\boldsymbol{e}_3)/\sqrt{2} & [\omega \cdot k_\parallel < 0 \quad \text{or} \quad (k_\parallel = 0 \quad \text{and} \quad \omega \cdot k_\perp < 0)] \end{cases}$$

$$E_l = \boldsymbol{E}(\boldsymbol{k}, \omega) \cdot \boldsymbol{e}_l \qquad E_r = \boldsymbol{E}(\boldsymbol{k}, \omega) \cdot \boldsymbol{e}_r, \tag{8}$$

where $\boldsymbol{E}(\boldsymbol{k}, \omega)$ is the electric field in the $\boldsymbol{k} - \omega$ space and is obtained via the FFT. With the definition of Equation (8), the polarization state of a wave also refers to the ambient magnetic field (Stix 1962; Gary 1993). Hence, the right- and left-handed polarized waves rotate in the same sense as an electron and a proton, respectively, as far as they propagate along (either parallel or antiparallel to) the ambient magnetic field. Also note that the wave and its polarization make no sense when $\omega = 0$ and/or $|k| = 0$. Hence, the contribution of $\omega = 0$ and/or $|k| = 0$ to the polarization is not considered in our calculations.

Following the definition of the Stokes parameters (McMaster 1954; Carozzi et al. 2001), for a wave at a given time, its circular polarization degree (CPD, P) can be calculated as

$$P = \frac{|E_r|^2 - |E_l|^2}{|E_r|^2 + |E_l|^2}, \tag{9}$$

where the vertical bars $|*|$ indicate the amplitude of the respective quantity. In order to determine the CPD, P, in a plasma (with many waves) at a given time or a wave over a period, instead of taking the average value of CPDs from different waves, we use

$$P = \frac{\langle|E_r|^2\rangle - \langle|E_l|^2\rangle}{\langle|E_r|^2\rangle + \langle|E_l|^2\rangle}, \tag{10}$$

where the angle brackets $\langle * \rangle$ indicate the average value of each corresponding quantity. Note that for different studies, averages are calculated in different spaces, i.e., (1) averages over the $\boldsymbol{k}$ space are considered for the evolution of the CPD, and (2) for CPD along a wave propagation direction θ with respect to $\boldsymbol{B}_0$, we take averages in both ω and $k_\parallel/k_\perp = \cos\theta$ spaces. The definition in Equation (10), hence, can give us a direct idea of which polarization is energetically dominant. We thus can verify that the polarization is circular with a right- or left-handed sense according to $P > 0$ or $P < 0$, respectively. A value of $P = 1(-1)$ corresponds to fully right-handed (left-handed) circular polarization, and $P = 0$ indicates a linear polarization.

In our diagnostics, magnetic fields are used to determine the energies of electromagnetic wave modes. Adopting magnetic fields can automatically filter out electrostatic waves since an electrostatic wave does not contain magnetic fluctuations. For calculations related to polarization, however, electric fields are used. Note that we will not investigate evolutions of the anisotropy and CPD, since the whole time duration of our simulations (dozens of microseconds) is much shorter than the time resolutions of the remote detectors (more than milliseconds).

3. Simulation Results

As mentioned in Section 2.2.1, the dispersion relation of magnetized cold plasmas will be applied to identify which wave has been excited. There are five different wave branches in the cold-plasma limit, while each mode branch (or surface) can be differently named for different frequencies and/or wave propagation directions (Andre 1985). For example, when waves propagate along the ambient magnetic field, the X mode is usually called the (right-handed polarized) R mode, while the O mode is associated with the (left-handed polarized) L mode. In this paper, however, we will simply call them ion-cyclotron, whistler, slow extraordinary (Z), ordinary (O), and fast extraordinary (X) modes from the low to high frequencies, respectively. For the applied physical proton-to-electron mass ratio $m_p/m_e = 1836$, the frequencies in the ion-cyclotron branch are marginally resolved in our calculations. In the following, we will ignore the ion-cyclotron branch.

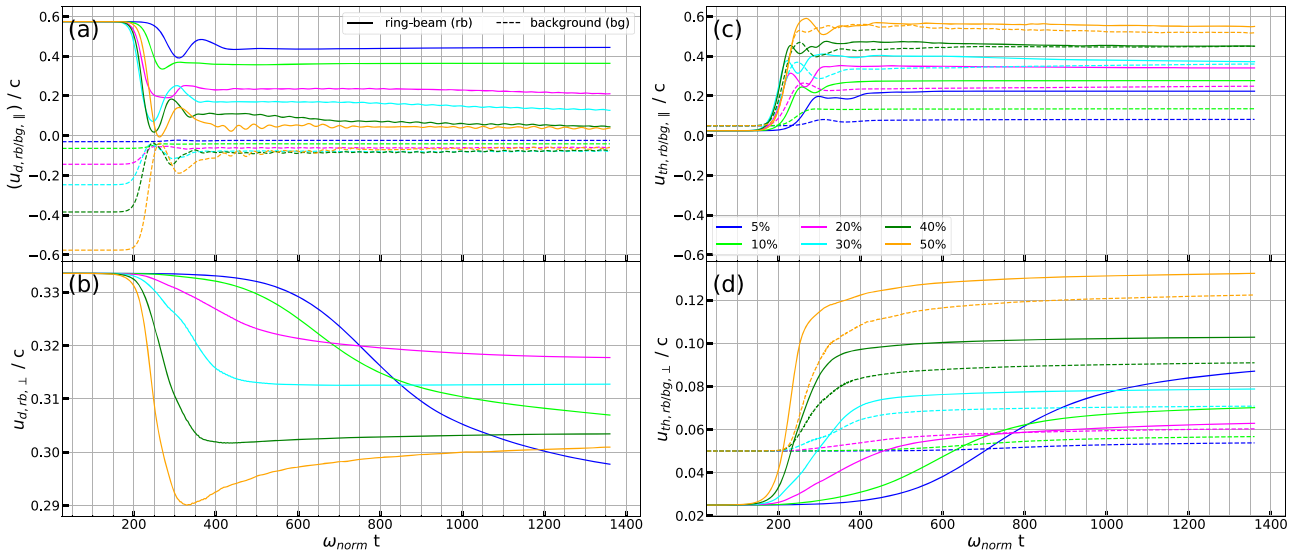

Figure 1. Evolutions of the bulk (or average, u_d) drift momenta and thermal spreads ($u_{\rm th}$) in the directions along (panels (a) and (c)) and perpendicular (panels (b) and (d)) to the ambient magnetic field $\boldsymbol{B}_0$ for both the ring-beam (rb; solid lines) and the background (bg; dashed lines) electrons, except for the perpendicular bulk drift momentum of the background electrons ($u_{d,{\rm bg},\perp}$), which is close to 0. In each panel, different colors are used to distinguish the different number density ratios between the ring-beam and total electrons $n_{\rm rb}/n_t$. Here $\omega_{\rm ce}/\omega_{\rm pe} = 5.0$, and all momenta are normalized by the speed of light c.

3.1. n_{rb}/n_t Dependence

In this section, the dependence of excited wave properties on the number density ratio between the ring-beam and total electrons $n_{\rm rb}/n_t$ is discussed. In addition, the ratio between the electron cyclotron frequency $\omega_{\rm ce}$ and the electron plasma frequency $\omega_{\rm pe}$ is fixed at $\omega_{\rm ce}/\omega_{\rm pe} = 5$.

Both beam and ECM instabilities can occur with the ring-beam momentum distribution. Note that many instabilities can fit with the description of the beam instability, since their free energy sources come from the drifting beam population, e.g., the reactive beam instability, kinetic Langmuir beam (or bump-in-tail) instability, whistler heat flux instability, firehose instability, etc. (Melrose 1986; Gary 1993). With the initial setup in this study (see Section 2.1), these instabilities may occur at the different stages of the free energy release. We will not distinguish these instabilities and call them simply the beam instability in this study.

3.1.1. Statistics of Particles

The beam and ECM instabilities, in general, are triggered by the electron free energies in the directions along and perpendicular to the ambient magnetic field $\boldsymbol{B}_0$, respectively. Evolution of the electron momentum along each direction can, hence, give us insights on the growth and saturation of these instabilities. Panels (a)–(d) of Figure 1 show the evolutions of the bulk (or average) drift momenta and thermal spreads in the directions along and perpendicular to $\boldsymbol{B}_0$ for both the ring-beam and background electrons, respectively. The bulk drift momentum and thermal spread of different electron species (s) along different directions (t) are defined as $u_{d,s,t} = (\sum_i u_{s,t,i})/N$ and $u_{{\rm th},s,t} = \sqrt{[\sum_i (u_{s,t,i}^2 - u_{d,s,t}^2)]/N}$, where $s =$ rb or bg for the ring-beam or background electrons, respectively, and $t = \parallel$ or $\perp$ for the direction along or perpendicular to $\boldsymbol{B}_0$, respectively. In addition, $u_{s,t,i}$ is the parallel or perpendicular momentum of a single electron i, and N is the total electron number in species s. The evolution of the perpendicular bulk drift momentum of the background electrons is not shown in Figure 1(b), since it is negligible compared to that of the ring-beam population. Note that we stopped our simulations when these quantities reach quasi-steady values, i.e., there is no obvious energy exchange between electromagnetic fields and particles.

Panels (a) and (b) of Figure 1 show the evolutions of the bulk drift momenta in the parallel and perpendicular directions, respectively. The first minima of these curves indicate the saturation of their corresponding instabilities. One can see that the reduction of the free energy, generally, is faster and larger in the parallel than in the perpendicular direction. The faster free energy reduction in the parallel direction implies that waves excited by the beam instability will saturate earlier than those by the ECM instability. (Note that, in this paper, the saturation of a wave corresponds to the end of the growth phase in its energy evolution profile.)

While the free energy release rates of the beam instability do not vary significantly among cases with dense ring-beam electrons ($n_{\rm rb}/n_t \geqslant 20\%$, Figure 1(a)), the free energy for the ECM instability decreases faster with the increase of the ring-beam electron population (Figure 1(b)). Moreover, the greater free energy reduction in the parallel direction implies that waves induced by the beam instability should contain more energy than those due to the ECM instability. This difference becomes larger with the increase of $n_{\rm rb}/n_t$.

Figure 1(a) shows that both the ring-beam and background electrons simultaneously lose their bulk drift energies along $\boldsymbol{B}_0$, making contributions to the wave excitation driven by the beam instability. Generally, in both the parallel and antiparallel directions, the release of the electron drift energy increases monotonically with the increase of $n_{\rm rb}/n_t$. Evolution of the bulk drift momentum of the ring-beam electrons in the direction perpendicular to $\boldsymbol{B}_0$ (Figure 1(b)) is, however, more complicated than that in the parallel direction, i.e., the decreases of the perpendicular bulk drift momentum in the cases with $n_{\rm rb}/n_t = 5\%$ and 10% are slower but even more significant than in the cases with $n_{\rm rb}/n_t \geqslant 20\%$. This indicates that different dynamic processes are underway between cases with $n_{\rm rb}/n_t \leqslant 10\%$ and $n_{\rm rb}/n_t \geqslant 20\%$, which we will clarify later.

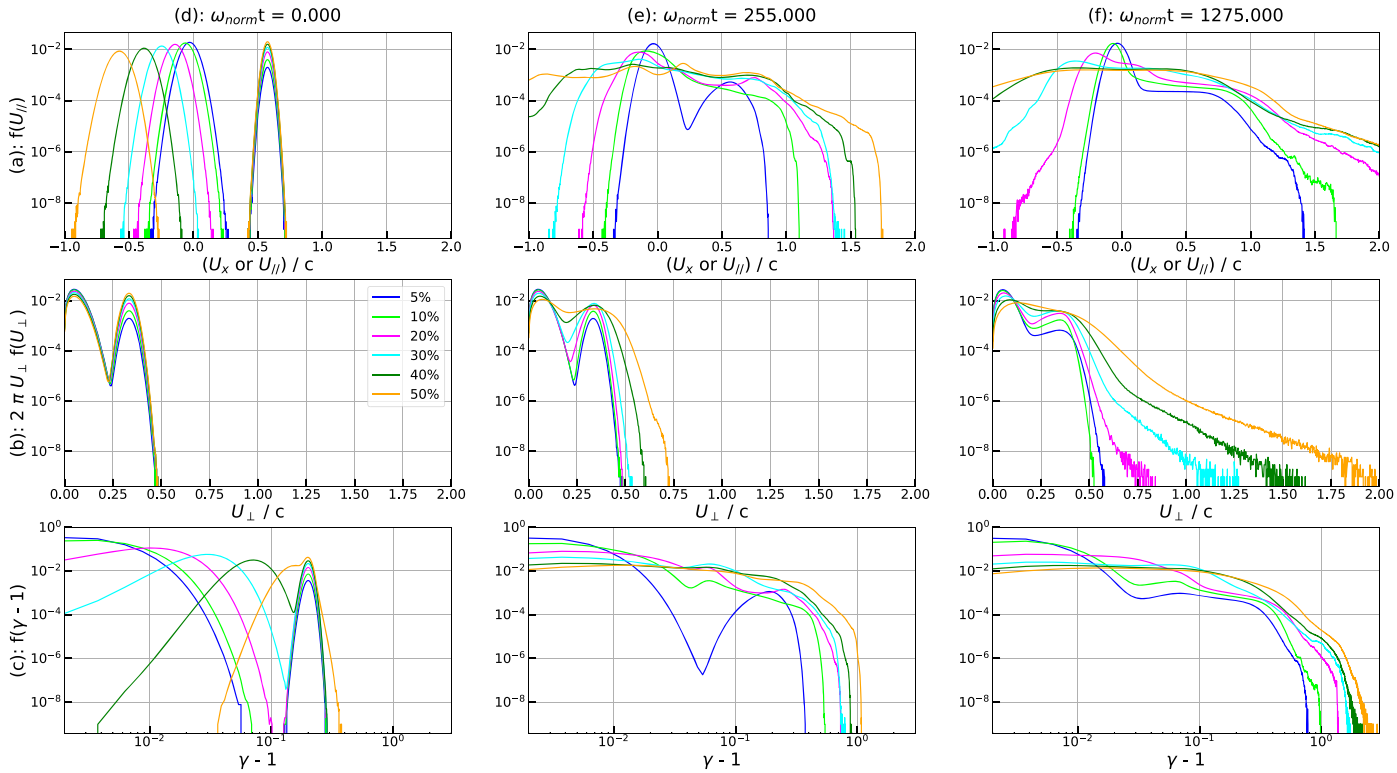

Figure 2. Distributions of the parallel momentum ($f(u_{//})$, row (a)), perpendicular momentum ($2\pi U_\perp f(u_\perp)$, row (b)) and total kinetic energy ($f(\gamma-1)$, row (c)) of all electrons at $t = 0.0$ (column (d)), $255\omega_{\rm norm}^{-1}$ (column (e)), and $1275\omega_{\rm norm}^{-1}$ (column (f)), corresponding to the initial condition, the time around when the parallel bulk drift momenta of the ring-beam electrons reach their minima (see Figure 1(a)), and the time close to the end of simulations. In each panel, different colors are used to distinguish the different number density ratios between the ring-beam and total electrons $n_{\rm rb}/n_t$. Here $\omega_{\rm ce}/\omega_{\rm pe} = 5.0$. All distributions are normalized by the number of all electrons.

Part of the released energies from the bulk drift motion are, however, absorbed again by electrons themselves via wave–particle interactions, leading to electron heating and acceleration. Electron thermal spread is, hence, strongly enhanced and has opposite behavior to its corresponding bulk drift motion in both parallel and perpendicular directions; see panels (c) and (d) of Figure 1. Especially in the direction along $\boldsymbol{B}_0$ (panel (c)), the final thermal spread of the ring-beam electrons already reaches a relativistic regime ($>0.4c$) in the cases with $n_{\rm rb}/n_t > 30\%$. For the case with $n_{\rm rb}/n_t = 50\%$, this is almost equal to its initial parallel drift momentum. In the final quasi-steady state, the thermal spread of the background electrons is, in general, smaller than that of the ring-beam electrons, and the thermal spread of all electrons is much wider in the parallel direction than in the perpendicular direction, which agrees with the distributions of the parallel and perpendicular momenta shown in Figure 2.

Figure 2 shows the evolutions of the parallel and perpendicular momentum and energy distributions of all electrons. One can see that when the plasma system is close to its quasi-steady state ($t = 1275\omega_{\rm norm}^{-1}$, column (f)), the initial free energies for the beam ($u_\parallel \cdot \partial f/\partial u_\parallel > 0$, row (a)) and ECM ($\partial f/\partial u_\perp > 0$, row (b)) instabilities are almost totally dissipated and plateau momentum distribution forms in all directions. Meanwhile, with panels in rows (a) and (b), strong electron acceleration can also be seen along each direction, particularly in the cases with larger $n_{\rm rb}/n_t$. Note that the high momentum tail in the antiparallel direction contains reflected ring-beam electrons and reflection of the ring-beam electrons is suppressed in cases with $n_{\rm rb}/n_t \leqslant 10\%$. The reflection of the ring-beam electrons makes the wave generation more symmetric with respect to the plane perpendicular to $\boldsymbol{B}_0$. Petrosian & Liu (2004) found that acceleration of particles via resonant wave–particle interactions can be enhanced significantly if particles can resonate with multiple waves simultaneously. Hence, reflection of the ring-beam electrons will increase their acceleration efficiency. This may explain the correlation between the ring-beam electron reflection and their acceleration in the perpendicular direction. Strong perpendicular acceleration also leads to the late increase of perpendicular drift momentum in the case with the maximum ring-beam electron density ($n_{\rm rb}/n_t = 50\%$ in Figure 1(b)). Interestingly, in each $n_{\rm rb}/n_t$ case, a double power-law distribution forms in the high-energy tail with $\gamma - 1 > 0.1 \sim 50$ keV when the plasma system is close to its quasi-steady state, i.e., after the releases of the free energies for both the beam and ECM instabilities. Their break energies are located around the initial energy ($\gamma \sim 1.2$) of the ring-beam electrons (see the bottom right panel in Figure 2).

3.1.2. Excited Electrostatic Waves

Based on the coordinates of our simulations, electric component E_z is purely transverse, while the characters of the E_x and E_y components change with wave propagation direction, i.e., E_x is a purely longitudinal (transverse) component when waves propagate along (perpendicular to) the ambient magnetic field $\boldsymbol{B}_0$, i.e., $\boldsymbol{k} \| \boldsymbol{B}_0$ and $\theta = 0^\circ$ or 180° ($\boldsymbol{k} \perp \boldsymbol{B}_0$ and $\theta = 90^\circ$ or 270°). But, in general, E_x and E_y represent a mixture of both longitudinal and transverse electric field components. Note that $\theta \leqslant 90^\circ$, together

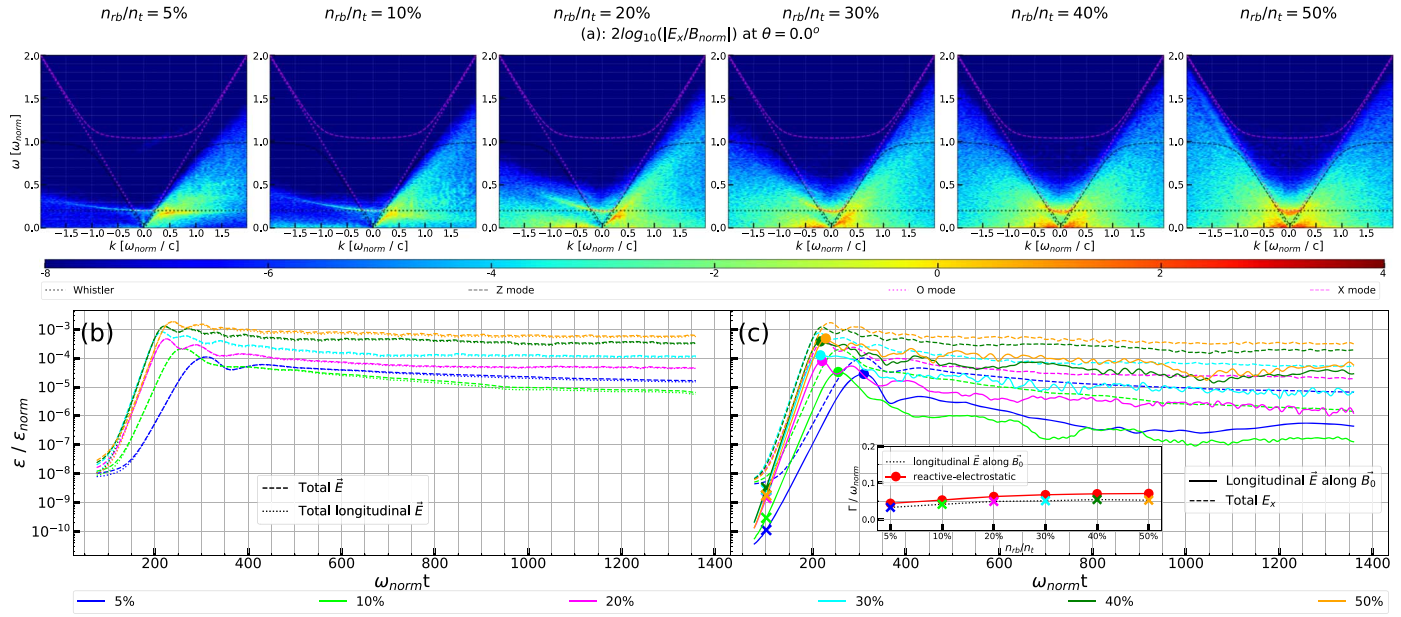

Figure 3. Row (a): wavevector–frequency ($\boldsymbol{k} - \omega$ or dispersion) spectra of electric component E_x of waves propagating along (either parallel $k > 0$ or antiparallel $k < 0$ to) the ambient magnetic field $\boldsymbol{B}_0$ ($\theta = 0°$). Different panels in row (a) are for different $n_{\rm rb}/n_t$ (from left to right column $n_{\rm rb}/n_t = 5\%$, 10%, 20%, 30%, 40%, 50%, respectively) and share the same contour scale, normalization $B_{\rm norm}$ (Section 2.1). In each panel of row (a) from the bottom to top, the overplotted lines are the whistler (black dotted lines), Z (black dashed lines), O (magenta dotted lines), and X (magenta lines) modes in magnetized cold plasmas, respectively. These $\boldsymbol{k} - \omega$ spectra are obtained via the FFT over the entire spacetime domain of our simulations. Panel (b) presents energy evolutions of the total electric fields (dashed lines) and total longitudinal electric fields (dotted lines) of all waves in the simulation domain. Panel (c) shows energy evolution of the longitudinal electric fields of waves propagating along $\boldsymbol{B}_0$ (solid lines), as well as that of the electric component E_x (dashed lines) in the whole simulation domain. The inset of panel (c) shows the fitted exponential growth rate of these $\boldsymbol{B}_0$-aligned longitudinal electric fields (black dotted line), as well as the theoretical maximum growth rate of the electrostatic waves by the reactive beam instability in unmagnetized cold plasmas (red solid line with circles; see Equation (11)). Fitted ranges for these growth rates are indicated by crosses and circles in the main part of panel (c). Different colors in panels (b) and (c) are used to distinguish cases with different $n_{\rm rb}/n_t$ but $\omega_{\rm ce}/\omega_{\rm pe} = 5.0$.

with the sign of $\pm k$, gives two supplementary wave propagation directions in the wave $\boldsymbol{k} - \omega$ (or dispersion) spectra of Figures 3, 4, 7, and 10.

Hence, in row (a) of Figure 3, one can mainly find excited electrostatic modes, i.e., Langmuir and (electron) beam modes. Hereinafter we define a wave mode being excited if its spectral intensity is significantly higher than that of an isotropic equilibrium Maxwellian plasma, which has the same thermal spread and $\omega_{\rm pe}$ as the background and total electrons in the ring-beam simulations (see Section 2.1), respectively, corresponding to $n_{\rm rb}/n_t = 0\%$ in Figures 5 and 6. Since the ECM instability, in general, mainly excites electromagnetic modes, the excitations of the electrostatic Langmuir and beam modes should be mostly due to the beam instability.

Similar to Karlický & Bárta (2009) and Ganse et al. (2012b), antiparallel-propagating Langmuir waves (L') are also excited in all ring-beam plasmas (see the left half of each panel in row (a) of Figure 3, where $\theta = 0°$ and $k < 0$). As mentioned in Section 1, generation of the L' waves could be attributed to electrostatic decay of the parallel-propagating Langmuir waves ($L \rightarrow L' + S$) and/or free energies for the beam instability in the antiparallel-drifting background electrons. In our simulations, we indeed found both intensity enhancement in the ion density fluctuation spectra for plasmas with dense ring-beam electrons $n_{\rm rb}/n_t \geqslant 20\%$ (similar to Figure 4 of Thurgood & Tsiklauri 2015) and reduction of the free energy in the antiparallel-drifting background electrons (see row (a) of Figure 2).

Furthermore, one can see the rise of these excited L' branches toward larger ω at a given wavenumber $k < 0$ with the increase of $n_{\rm rb}/n_t$, which agrees with a higher effective electron temperature of the antiparallel-moving electrons in plasmas with a larger $n_{\rm rb}/n_t$ (Figure 1(c)), since higher electron temperature will lead to a larger slope ($d\omega/dk$) in the dispersion relation of the Langmuir wave, i.e., $\omega^2 = \omega_{\rm pe}^2 + 3k^2v_{\rm the}^2$, where $v_{\rm the} \propto \sqrt{T_e}$ is the effective thermal velocity of electrons. Correspondingly, excitation of the L' waves appears at increasingly smaller wavenumbers $|k|$. That could be due to electron Landau damping (Landau 1946; Tsurutani & Lakhina 1997) of longitudinal electric fluctuations with large $|k|$ in hot plasmas, where Langmuir waves will get damped when their $|k|$ become larger than $1/\lambda_{\rm De}$ ($\lambda_{\rm De} \propto \sqrt{T_e}$ and T_e is the effective electron temperature).

In the direction antiparallel to $\boldsymbol{B}_0$, except for the L' wave, intensity of the beam mode $\omega = kv_b < \omega_{\rm pe}$ is also enhanced. The typical drift velocity v_b of these excited antiparallel-propagating beam modes also increases with the increase of $n_{\rm rb}/n_t$, since initially we have $u_{\rm bg\parallel} = -u_{\rm rb\parallel}n_{\rm rb}/n_{\rm bg}$, i.e., the initial bulk drift momentum of the background electrons $u_{\rm bg\parallel}$ increases with the increase of $n_{\rm rb}/n_t$ (see dashed lines at $t = 0$ in Figure 1(a)).

In the direction parallel to $\boldsymbol{B}_0$ ($\theta = 0°$ with $k > 0$ in row (a) of Figure 3), similar to the conditions in the antiparallel direction, enhanced intensities of both the parallel-propagating Langmuir (L) and beam modes can be found in each $n_{\rm rb}/n_t$ case. And also, due to the Landau damping in hot plasmas, these excited L waves are confined to smaller $|k|$ with the increase of $n_{\rm rb}/n_t$. Landau damping of small-scale longitudinal electric fluctuations will lead to electron heating discussed in Section 3.1.1. While different from those antiparallel-propagating beam modes, the typical drift velocity v_b of the excited

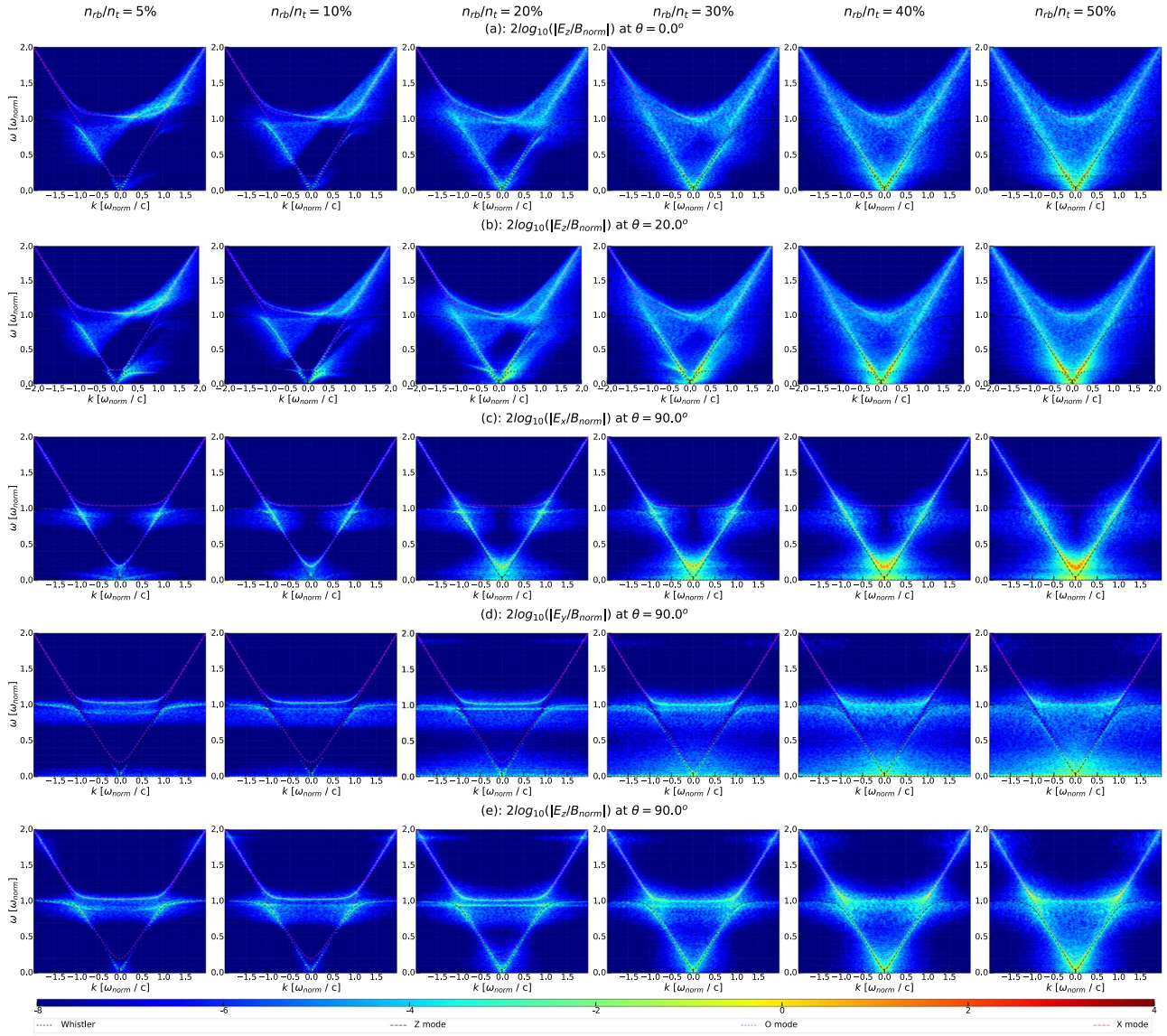

Figure 4. $\boldsymbol{k} - \omega$ spectra of different electric field components for different $n_{\rm rb}/n_t$ (from left to right columns $n_{\rm rb}/n_t = 5\%$, 10%, 20%, 30%, 40%, 50%, respectively) and wave propagation directions θ (row (a): E_z with $\theta = 0°$; row (b): E_z with $\theta = 20°$; row (c): E_x with $\theta = 90°$; row (d): E_y with $\theta = 90°$; row (e): E_z with $\theta = 90°$) with $\omega_{\rm ce}/\omega_{\rm pe} = 5.0$. In each panel, overplotted lines, contour scale, and normalization are the same as those in row (a) of Figure 3.

parallel-propagating beam modes, however, decreases with the increase of $n_{\rm rb}/n_t$ owing to the stronger reduction of the parallel bulk drift energy of the ring-beam electrons in cases with larger $n_{\rm rb}/n_t$ (see solid lines in Figure 1(a)).

By comparing these electrostatic waves in the $\theta = 0°$ and 180° directions (row (a) of Figure 3), one can see that intensities of the parallel-propagating Langmuir and beam modes are generally stronger than the antiparallel-propagating ones for each $n_{\rm rb}/n_t$ case. This difference is, however, reduced with the increase of $n_{\rm rb}/n_t$, since the free energy for the beam instability from the antiparallel-moving background electrons becomes comparable to that from the parallel-moving ring-beam electrons with the increase of $n_{\rm rb}/n_t$. Moreover, for high ring-beam density cases with $n_{\rm rb}/n_t \geqslant 20\%$, a significant fraction of the ring-beam electrons can be reflected, which also makes the wave excitation more symmetric with respect to the perpendicular plane. Additionally, besides linear waves as indicated by the cold-plasma dispersion relations, diffusive nonlinear electrostatic waves are also excited.

Figure 3(b) shows energy evolutions of the total electric fields $(\sum_{x,y}[\boldsymbol{E}(x, y)]^2\Delta x\Delta y)$ and total longitudinal electric fields $(\sum_{\boldsymbol{k}}[(\boldsymbol{E}(\boldsymbol{k})\cdot\boldsymbol{k})/|k|]^2\Delta\boldsymbol{k})$ of all waves in the simulation domain, where $\boldsymbol{E}(\boldsymbol{k})$ is the electric field vector of waves with wavevector $\boldsymbol{k}$. Note that the total longitudinal electric fields contain not only electric fields of electrostatic waves but also the longitudinal electric component of the electromagnetic waves. One can see that, for each $n_{\rm rb}/n_t$ case, the total longitudinal electric component occupies most of the total electric field energy (their energy evolution profiles are almost overlapped with each other): it is over one order of magnitude larger than the transverse electric field energy, which is shown in Figure 7(e). A similar result had also been found by Lee et al. (2009).

Energy evolutions for the electric component $E_x(x, y)$ $(\sum_{x,y}[E_x(x, y)]^2\Delta x\Delta y)$ and the longitudinal electric fields of waves propagating along $\boldsymbol{B}_0$ $(\sum_{k_\perp=0}[(\boldsymbol{E}(\boldsymbol{k})\cdot\boldsymbol{k})/|k|]^2$, i.e., waves shown in row (a) of Figure 3) are presented in Figure 3(c).

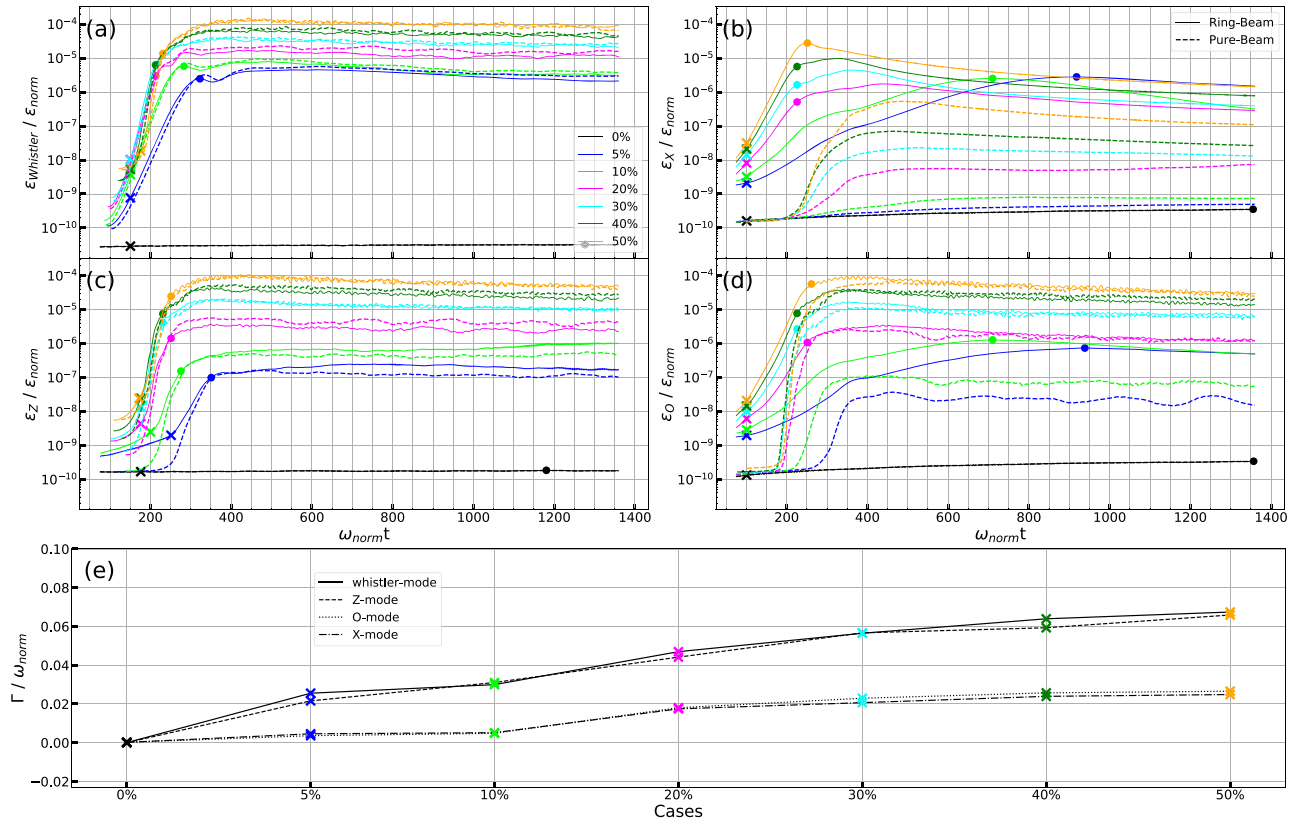

Figure 5. Magnetic energy evolutions of the electromagnetic whistler ($\varepsilon_{\rm whistler}$, panel (a)), X ($\varepsilon_X$, panel (b)), Z ($\varepsilon_Z$, panel (c)), and O ($\varepsilon_O$, panel (d)) modes, where solid (dashed) lines are for plasmas with energetic ring-beam (pure-beam) electrons and $\omega_{\rm ce}/\omega_{\rm pe} = 5.0$. Panel (e) shows the fitted exponential growth rates of these four electromagnetic wave modes for plasmas with energetic ring-beam electrons but different $n_{\rm rb}/n_t$ (distinguished with different colors). The solid, dashed, dotted, and dashed–dotted lines in panel (e) are for the whistler, X , Z, and O modes, respectively. And fitted ranges for these growth rates are indicated by crosses and circles in their corresponding panels (panels (a) to (d)).

One can see that the energy of $E_x(x, y)$ is comparable to the total longitudinal electric fields. And the energy of the $\boldsymbol{B}_0$ aligned longitudinal electric fields is a factor of a few lower except in the early phase of these simulations, when the energy of the total longitudinal electric fields appears to be isotropic (especially at $t = 0$) and dominated by nonparallel-propagating waves. To validate our simulations, in the inset of panel (c) we compare the growth rate of these $\boldsymbol{B}_0$-aligned longitudinal electric fields to the maximum growth rate of electrostatic waves by the beam instability in the nonresonant fluid or reactive regime of unmagnetized plasmas (i.e., in cold unmagnetized plasmas). These two growth rates should agree with each other, since the $\boldsymbol{B}_0$-aligned longitudinal electric fields are dominated by electrostatic waves (see row (a) of Figure 3) and these electrostatic waves are mainly excited by the beam instability. Moreover, in magnetized plasmas, excitation of the electrostatic waves propagating along the ambient magnetic field is exactly the same as that in unmagnetized plasmas (see Gary 1993, chap. 3.3). Additionally, the setup of our simulations is also located in the reactive regime with $(n_{\rm rb}/n_t)^{1/3}(u_{\rm rb\parallel}/u_{\rm th\parallel}) \gg 1$, where $(n_{\rm rb}/n_t)^{1/3}(u_{\rm rb\parallel}/u_{\rm th\parallel})$ is a measure of the reactive ($\geqslant$1) or kinetic ($<$1) nature of the beam instability (Melrose 1986; Gary 1993; Melrose 2017).

The maximum growth rate of the electrostatic waves due to the reactive beam instability was obtained from the dispersion equation for unmagnetized plasmas by setting the longitudinal dielectric element $K^L(\omega, \boldsymbol{k})$ to be zero. In the unmagnetized cold-plasma limit ($u_{\rm rb\parallel} \gg u_{\rm th\parallel}$, Equation (2.16) in Melrose 1986), that is

$$K^L(\omega, \boldsymbol{k}) = 1 - \Sigma_s \frac{q^2 n_s}{\varepsilon_0 \gamma_s m_s \omega^2} \times \left[1 + \frac{2\boldsymbol{k}\cdot\boldsymbol{v}_{ds}}{\omega - \boldsymbol{k}\cdot\boldsymbol{v}_{ds}} + \frac{1 - \omega^2/(k^2c^2)}{(\omega - \boldsymbol{k}\cdot\boldsymbol{v}_{ds})^2}(\boldsymbol{k}\cdot\boldsymbol{v}_{ds})^2\right] = 0, \quad (11)$$

where Σ_s is for a summing over all particle species (s) in plasma and v_{ds}, $\gamma_s = (1 - v_{ds}^2/c^2)^{-1/2}$ are the bulk drift velocity and its corresponding gamma factor of particle species s, respectively. When $n_{\rm rb} \ll n_t$, one can get the growth rate of the classical weak-beam instability from Equation (11): $\Gamma/\omega_{\rm pe} = \sqrt{3}\,(n_{\rm rb}/n_{\rm bg})^{1/3}/2^{4/3}$ (see Equation (3.2.9) in Gary 1993). The growth rate of the electrostatic waves propagating along $\boldsymbol{B}_0$ in our simulations is evaluated via a linear fit in the range indicated by crosses and circles in panel (e). One can see that the growth rate of the electrostatic waves propagating along $\boldsymbol{B}_0$ is generally slightly smaller than the theoretical maximum one by the reactive beam instability. Similar results were also found in the study of Karlický & Bárta (2009). On the one hand, this could be due to the free energy reduction of the energetic ring-beam electrons, i.e., effective $n_{\rm rb}$ and $u_{\rm rb\parallel}$ for the reactive beam instability will decrease with the wave excitation. Small effective $n_{\rm rb}$ and $u_{\rm rb\parallel}$ lead to a smaller growth rate for the reactive beam instability (Gary 1993). On the other hand, particles can

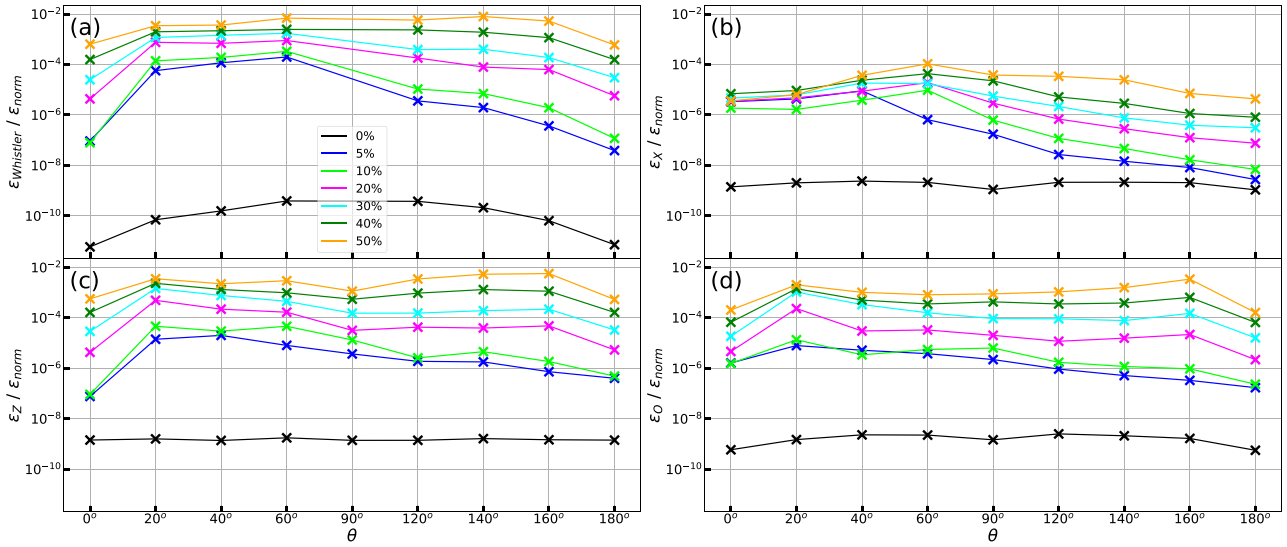

Figure 6. Anisotropic magnetic energies (Equation (6)) of the electromagnetic whistler ($\varepsilon_{\rm whistler}$, panel (a)), X ($\varepsilon_X$, panel (b)), Z($\varepsilon_Z$, panel (c)), and O ($\varepsilon_O$, panel (d)) modes with $\omega_{\rm ce}/\omega_{\rm pe} = 5.0$. Different colors in each panel are for different $n_{\rm rb}/n_t$.

simultaneously absorb some waves during the wave excitations (i.e., plasma heating by Landau damping; see Figure 1(c)), and increased electron momentum spread (or temperature) can also reduce the growth rate of the reactive beam instability (see Section 3.4 in Melrose 1986). Additionally, not all electrostatic waves propagating along $\boldsymbol{B}_0$ grow with the theoretical maximum rate of the reactive beam instability. Generally, values of the growth rate of the electrostatic waves propagating along $\boldsymbol{B}_0$ are quite similar to those of the whistler mode (Figure 5(e)), which is also consistent with the study of Lee et al. (2011).

3.1.3. Excited Electromagnetic Waves

Figure 4 shows the electric field dispersion spectra of electromagnetic waves along different wave propagation directions θ (=0° or 20° or 90°). Due to the rotational symmetry in the direction perpendicular to the ambient magnetic field $\boldsymbol{B}_0$, dispersion spectra of E_y and E_z are very similar for waves with $k_\perp = 0$ (row (a)), and the dispersion spectra of waves with $k_\parallel = 0$ are symmetric with respect to $k_\perp = 0$ (rows (c) to (e)).

Excitations of all electromagnetic whistler, Z, O, and X modes can be found in the purely transverse electric component E_z spectra along $\boldsymbol{B}_0$ (row (a) of Figure 4). Similar to the electrostatic component E_x along $\boldsymbol{B}_0$ (row (a) of Figure 3), there is also an asymmetry on the transverse electric intensity of waves oppositely propagating along $\boldsymbol{B}_0$, especially for plasmas with tenuous ring-beam electrons. It is interesting to note that the X (Z) mode dominates the transverse electric field spectra in the direction parallel (antiparallel) to $\boldsymbol{B}_0$ with tenuous ring-beam electrons. Between the excited X and Z modes, there are also diffusive nonlinear waves that do not follow the dispersion relations of the linear waves in the cold-plasma limit. With the increase of $n_{\rm rb}/n_t$, excitations of the X and Z modes, as well as the whistler and O modes, become more and more symmetric with respect to the $\boldsymbol{B}_0$ perpendicular plane. The enhanced excitation of the antiparallel-propagating X mode in plasmas with dense ring-beam electrons may be caused by reflected ring-beam electrons (see row (a) of Figure 2), while the intensity of the parallel-propagating X-mode waves appears to be saturated. Along $\boldsymbol{B}_0$, the excitations of the whistler, Z, and O modes are inefficient for plasmas with tenuous ring-beam electrons, in contrast to the dense ring-beam cases.

For obliquely propagating electromagnetic waves with $\theta = 20°$ and 160° (row (b) of Figure 4), their transverse electric component E_z spectra have similar properties to those of the parallel- and antiparallel-propagating electromagnetic waves (in row (a)). E_z intensities of these excited obliquely propagating electromagnetic waves are, however, enhanced compared to those of the $\boldsymbol{B}_0$-aligned electromagnetic waves, especially in the whistler and Z modes.

Rows (c) to (e) of Figure 4 show the dispersion spectra of the electric components E_x, E_y, and E_z, respectively, for perpendicular-propagating electromagnetic waves. The whistler branch is absent in these panels, since its resonance or maximum frequency $\omega_W^{\rm res} \to 0$ at $\theta = 90°$ and 270° with the physical proton-to-electron mass ratio $m_p/m_e = 1836$ in the magnetized cold-plasma limit (Melrose 1986; Stix 1992). It is well known that the electric field of the O (Z and X) mode is parallel (perpendicular) to $\boldsymbol{B}_0$, when they propagate in the direction perpendicular to $\boldsymbol{B}_0$, i.e., $\boldsymbol{k} \perp \boldsymbol{B}_0$. In row (c), hence, one can find a strong O-mode excitation. The strong Z- and X-mode excitations, on the other hand, appear in the E_y and E_z spectra (rows (d) and (e)). The transverse electric E_z components of the Z and X modes contain more energies than their longitudinal electric E_y components. Generally, similar to the electrostatic modes (row (a) of Figure 3), intensities of the O, Z, and X modes also increase with the increase of $n_{\rm rb}/n_t$ in the plane perpendicular to $\boldsymbol{B}_0$.

In rows (d) and (e) of Figure 4, the X mode appears to be enhanced just below the second harmonic of $\omega_{\rm ce}$, and there is, additionally, an excited horizontal band located around $\omega_{\rm ce}$ and below the cutoff frequency of the X mode $\omega_X^{\rm cut} = (\omega_{\rm ce} + \sqrt{\omega_{\rm ce}^2 + 4\omega_{\rm pe}^2})/2 \approx 1.04\omega_{\rm norm}$. Following Pritchett (1984), we call this horizontal band the (electromagnetic) relativistic Bernstein mode. This mode results from the relativistic corrections to the classical dispersion of the magnetized cold-plasma approximation; see Pritchett (1984) for more details. This relativistic

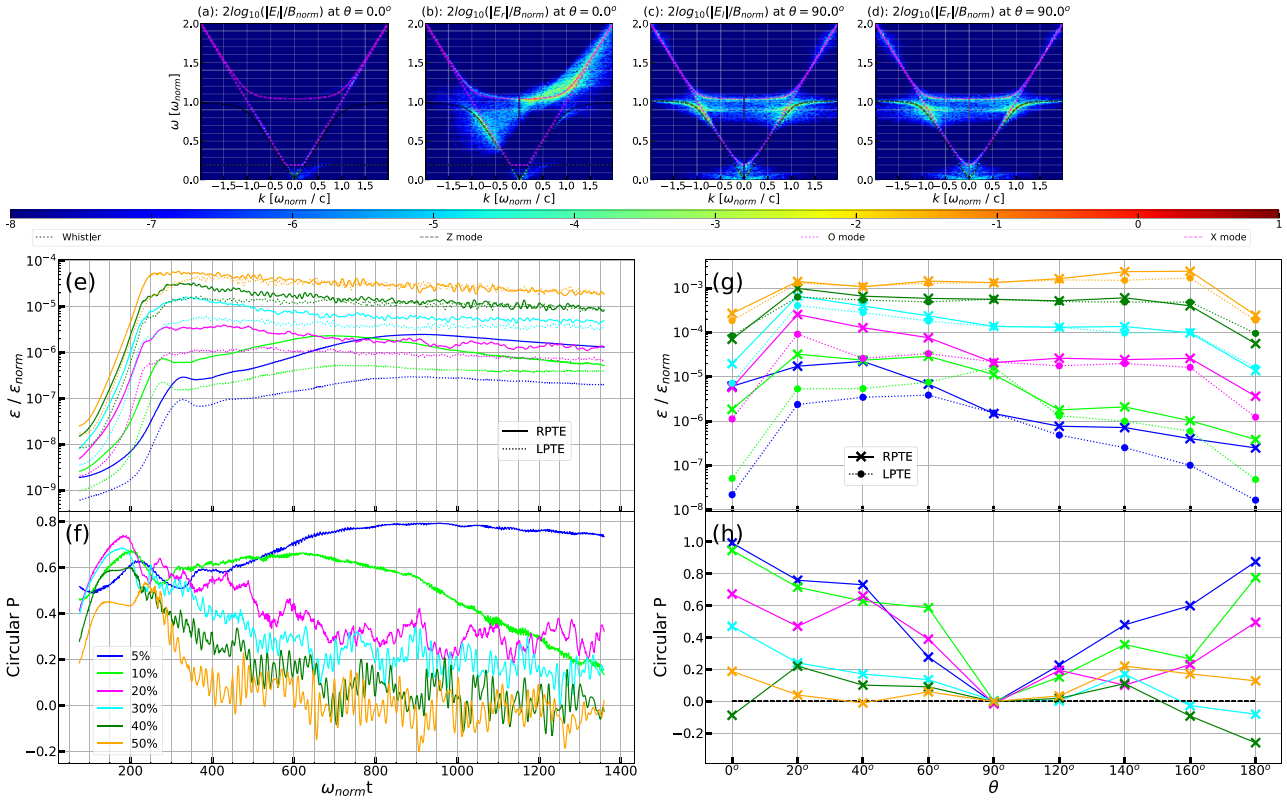

Figure 7. Panels (a)–(d) show the $\boldsymbol{k} - \omega$ spectra of the LPTE (E_l, panels (a) and (c)) and RPTE (E_r, panels (b) and (d)) of electromagnetic waves propagating along $\theta = 0°$ (panels (a) and (b)) and 90° (panels (c) and (d)), respectively, in plasmas with $n_{\rm rb}/n_t = 5\%$. These four panels share the same color bar. Overplotted lines and normalization in these four panels are the same as those in Figures 3 and 4. Energy evolutions of the RPTE (solid lines) and LPTE (dotted lines) of all electromagnetic waves in the simulation domain are presented in panel (e). Panel (f) shows the CPD evolution of these transverse electric fields. Dependences of the energies of the RPTE (solid lines with crosses), LPTE (dotted lines with circles), and the CPD on the wave propagation direction θ are shown in panels (g) and (h), respectively, for transverse electric fields of all electromagnetic waves in the simulation domain. Different colors in each of panels (e) to (h) are used to distinguish the different $n_{\rm rb}/n_t$ cases, but all cases have $\omega_{\rm ce}/\omega_{\rm pe} = 5.0$.

Bernstein mode is, however, evident only in the cases with $n_{\rm rb}/n_t = 5\% - 30\%$, and the central frequency of this excited relativistic Bernstein mode increases with the increase of $n_{\rm rb}/n_t$. The absence of this horizontal mode in the cases with $n_{\rm rb}/n_t > 30\%$ could be due to merging of the X and Bernstein modes. Based on Figure 1 in Pritchett (1984), one can see that the cutoff frequencies of the X and Bernstein modes can be the same and above $\omega_{\rm ce}$ in plasmas with electron temperature above $0.1c$. In other words, the merging of the X and Bernstein modes indicates that the effective electron temperature could be higher than $0.1c$ (i.e., efficient heating occurs) in the cases with $n_{\rm rb}/n_t > 30\%$.

3.1.4. Electromagnetic Wave Energy

Since solar radio emissions are electromagnetic waves, we will mainly concentrate on properties of the electromagnetic whistler, Z, O, and X modes in the following. Section 3.1.3 shows that these four mode branches dominate the excited electromagnetic waves and roughly follow the dispersion relations of a magnetized cold plasma. Following the Gaussian filter method described in Section 2.2.1, we extract the magnetic energy carried by each branch of these four electromagnetic modes.

Panels (a)–(d) of Figure 5 show the evolutions of the magnetic energies of the whistler, X, Z, and O modes, respectively, where the case with $n_{\rm rb}/n_t = 0\%$, an equivalent isotropic thermal plasma, shows how much these whistler-, Z-, O-, and X-mode waves are enhanced with respect to their corresponding thermal levels. Note that, in numerical simulations, the whistler-, Z-, O-, and X-mode waves can also be seen in isotropic thermal plasmas without a source of free energy, which is due to the thermal noise numerically enhanced by the finite number of macroparticles (Kilian et al. 2017). Moreover, in Figure 5, the solid (dashed) lines represent the plasmas with a ring-beam (pure-beam) momentum distribution of energetic electrons. Differences in the magnetic energy evolutions between the ring-beam and the associated pure-beam momentum distributions are used to assess the effects of the ring feature in the ring-beam momentum distribution.

By comparing the magnetic energy evolutions between the ring-beam and the equivalent isotropic thermal plasmas, one can see that the saturation of each mode is over three orders of magnitude larger than their corresponding thermal levels. However, these magnetic energies are about one order of magnitude lower than the electric energy of the electrostatic waves propagating along $\boldsymbol{B}_0$ shown in Figure 3(c). All excited waves in the simulation domain are therefore dominated by electrostatic waves. Comparing the results of the ring-beam and pure-beam simulations, one can see that while the whistler mode appears to be mostly driven by the beam instability, the growths of the Z, O, and X modes have two components, especially in plasmas with tenuous ring-beam electrons. Moreover, in ring-beam plasmas, the onsets of the Z-, O-, and X-mode growth appear to be dominated by the ECM instability. The beam instability has delayed contributions to

the excitations of the Z, O, and X modes. For each wave mode, this delay decreases with the increase of the ring-beam electron density. In a plasma, this delay appears to increase with the increase of wave frequency. The beam instability, hence, tends to excite low-frequency waves first.

The saturation of the Z mode is, however, dominated by the beam instability in ring-beam plasmas. The same is true for O modes with dense ring-beam electrons ($n_{\rm rb}/n_t \geqslant 20\%$). For $n_{\rm rb}/n_t \leqslant 10\%$, the O-mode saturation is governed by the ECM instability and similar to the saturation time of the X mode, which corresponds well to the slow dissipation rate of the free energies in the direction perpendicular to the ambient magnetic field $\boldsymbol{B}_0$ (see Figure 1(b)) in the cases with $n_{\rm rb}/n_t \leqslant 10\%$. For the X mode, as predicted by the classical plasma emission theory, pure-beam distribution alone cannot lead to an efficient excitation of the X mode in plasmas with tenuous pure-beam electrons. On the other hand, with dense pure-beam electrons (e.g., $n_{\rm pb}/n_t = 50\%$, where $n_{\rm pb}$ is the number density of the pure-beam electrons), generation of the X mode can also saturate at a quite high energy.

Note that the magnetic energy envelope of the X mode in the case with ring-beam electrons $n_{\rm rb}/n_t = 5\%$ and $\omega_{\rm ce}/\omega_{\rm pe} = 5$ (blue solid line in panel (b)) is almost the same as those (Figure 4(i)) in the study of Lee et al. (2011).

Generally, the magnetic energy saturations of the whistler, Z, and O modes are enhanced with increasing ring-beam electron population (i.e., larger $n_{\rm rb}/n_t$). But for the X mode with the ring-beam momentum distribution, its magnetic energy saturations in the cases with $n_{\rm rb}/n_t = 5\%$ and 10% are not the smallest ones, since the free energies released from the perpendicular bulk drift momenta are, correspondingly, not the least in these two cases (see Figure 1(b)). Furthermore, in the ring-beam plasmas with the same $n_{\rm rb}/n_t$, the whistler mode has larger magnetic energy saturation than the other three (Z, O, and X) modes. Saturations of the Z-, O-, and X-mode waves decrease in that order when $n_{\rm rb}/n_t \geqslant 20\%$, which implies that wave excitation is more efficient at lower frequencies in plasmas with dense ring-beam electrons. For $n_{\rm rb}/n_t \leqslant 10\%$, the X mode can, however, have a larger saturation than the Z and O modes, and the saturation of the Z mode becomes the least among the Z, O, and X modes owing to contributions from the ECM instability.

In general, Figures 1 and 5 are well corrected and can be used to study energy exchange between waves and electrons. Due to the presence of waves and dynamic energy exchanges between particles and waves, the magnetic energy saturations of these electromagnetic wave modes are not exactly the same as the saturation time of their dominating instabilities (indicated by the formation of a plateau in their corresponding momentum distribution functions). In particular, a small positive gradient still remains in the perpendicular momentum distribution close to the end of simulations for plasmas with tenuous ring-beam electrons (panels (b)–(f) of Figure 2). Since the growth rates of the beam and ECM instabilities are proportional to the positive gradients of their corresponding distributions, their growth rates will become smaller when those gradients (free energy sources) are reduced (dissipated). When the gain of wave energy (due to instabilities) is equal to its losses (to heat plasma or accelerate particles), the wave energy will stop increasing and its energy saturation will be reached, no matter whether free energies for the instabilities remain or not. Moreover, the energy exchange between particles and waves can also lead to electron acceleration and heating: the increase of the electron perpendicular momentum in plasmas with dense ring-beam electrons (row (b) of Figure 2) is likely caused by cyclotron resonances, while the spread of the electron distribution in the parallel direction is dominated by Landau damping (row (a) of Figure 2). The nonlinear dynamic coupling between waves and particles is simplified or ignored in most of theoretical models. But they can be self-consistently recovered in fully kinetic PIC simulations.

Figure 5(e) shows the fitted growth rates of all four electromagnetic (whistler, X, Z, and O) modes in the ring-beam plasmas with different $n_{\rm rb}/n_t$, although these magnetic energies do not increase exactly exponentially with the time. The fitted ranges for these growth rates are shown in their corresponding panels of Figure 5. As one can see, the growth rate of each wave mode monotonously increases with the increase of $n_{\rm rb}/n_t$, in agreement with the theoretical predictions for the growth rates of the O and X modes (e.g., Freund et al. 1983; Wu & Freund 1984). In addition, with the fitted ranges we used, the growth rates between the whistler and Z (as well as O and X) modes are quite similar, probably due to the same dominant beam (ECM) instability during their growth phases. And the whistler mode always has a larger growth rate than the X mode, which is consistent with the study of Lee et al. (2011).

Additionally, we also study anisotropies of the whistler-, Z-, O-, and X-mode magnetic energies, as shown in Figure 6. In each panel, the total magnetic energy of an electromagnetic mode, covering the whole simulation domain and time series, is divided among the different wave propagation directions θ (Equation (6)). Considering the rotational symmetry of the system in the plane perpendicular to the ambient magnetic field $\boldsymbol{B}_0$ we only need to investigate dependence of the energy on θ from 0° to 180°. Note that the magnetic energy of the whistler mode at $\theta = 90°$ is not included in panel (a) owing to its resonance frequency $\omega_W^{\rm res} \to 0$ at $\theta = 90°$ with the physical proton-to-electron mass ratio $m_p/m_e = 1836$ in the magnetized cold-plasma limit.

Contrary to the electrostatic waves (Figure 3), magnetic energies are dominated by nonparallel electromagnetic waves. In plasmas with tenuous ring-beam electrons, the energy-dominated waves of all mode branches propagate in the same side as the ring-beam electron propagating (i.e., $\theta < 90°$). The anisotropies of the whistler, Z, and O modes decrease with the increase of the ring-beam electron density, while the anisotropy of the X mode is always high. In plasmas with dense ring-beam electrons, the X-mode magnetic energy has a stronger anisotropy than the other three (whistler, Z, and O) modes. The X mode is the strongest around $\theta = 60°$, indicating influences from the beam instability on the excitation of the X mode, since the strongest energy of the X mode is exactly located at $\theta = 90°$, when the energetic electrons initially follow a pure-ring momentum distribution (Pritchett 1984). In isotropic thermal plasmas (i.e., with $n_{\rm rb}/n_t = 0\%$), the magnetic energies of the whistler-, Z-, O-, and X-mode waves are much smaller than the excited ones by ring-beam electrons and more or less isotropic except for the whistler mode, which has (about one order of magnitude) less magnetic energy than the other three wave modes, but its anisotropy is the strongest.

Consistent with row (a) of Figure 4, in the directions along $\theta = 0°$ and 180°, wave excitation is dominated by the X and Z modes, respectively, in plasmas with tenuous ring-beam electrons. And energies of the obliquely propagating whistler

and Z modes with $\theta = 20°$ and 160° are larger than those of the $\boldsymbol{B}_0$-aligned ones (rows (a) and (b) of Figure 4, respectively). Along with the increase of the ring-beam electron density, magnetic energy of each electromagnetic mode increases in directions both along (row (a) of Figure 4) and perpendicular to (rows (c) and (e) of Figure 4) the ambient magnetic field $\boldsymbol{B}_0$, except for the quasi-parallel-propagating X-mode waves, which appear to be saturated as discussed for rows (a) and (b) of Figure 4 in Section 3.1.3.

We note that, with the Gaussian filter method, magnetic energy for each wave mode in Figures 5 and 6 might contaminate each other when the dispersion relations of two wave modes are close to each other. For example, row (a) of Figure 4 shows that, in plasmas with tenuous ring-beam electrons $n_{\rm rb}/n_t \leqslant 10\%$, the energy of the O mode propagating in the parallel (antiparallel) direction can have contributions from the X (Z) mode. The growth of the O mode in plasmas with tenuous ring-beam electrons (Figure 5(d)), therefore, may be influenced by these effects. This can be clearly seen in the following section when we consider the polarization of these waves.

3.1.5. Polarization Properties

The polarization of a wave depends on its propagation direction θ (Melrose 1986). When propagating parallel to $\boldsymbol{B}_0$ (i.e., $\theta = 0°$), the O-mode (X-mode) waves are fully left-handed (right-handed) circularly polarized and the Z-mode waves are fully left-handed (right-handed) circularly polarized when their frequencies $\omega < (>)\ \omega_{\rm pe}$ (see panels (a) and (b) of Figure 7). When $\theta = 90°$, both O- and X-mode waves are linearly polarized (see panels (c) and (d) of Figure 7, as well as rows (c) to (e) of Figure 4), since the electric fields of the O-mode (X-mode) waves are parallel (perpendicular) to $\boldsymbol{B}_0$.

Following the method described in Section 2.2.2, we separate the energies contained by the left- and right-handed polarized transverse electric fields (LPTE and RPTE) in electromagnetic waves. Figure 7(e) shows the energy evolutions of the LPTE and RPTE for all electromagnetic waves in the simulation domain. In the $n_{\rm rb}/n_t \leqslant 10\%$ cases, energy evolution profiles of the LPTE and RPTE contain two growth phases, indicating that both the beam and ECM instabilities play roles in the excitation of the electromagnetic waves in the simulation domain. These two growth phases correspond well to the obviously different dissipation rates of the free energies along the parallel and perpendicular directions for the beam and ECM instabilities, respectively (see panels (a) and (b) of Figure 1 and Figure 5). In general, in each $n_{\rm rb}/n_t$ case, the RPTE dominates the transverse electric field energy during most of the simulation time, due to the energy dominance of the right-handed polarized whistler and X-mode waves; see Figure 5.

Figure 7(f) shows the evolution of the CPD (Equation (10)) for all electromagnetic waves in the simulation domain. Due to the dominance of the RPTE in each $n_{\rm rb}/n_t$ case, all CPDs are positive at the beginning and increase during the wave growth phase. However, they start to decrease after the energy saturation of the transverse electric fields. For larger $n_{\rm rb}/n_t$ cases, the CPDs can be close to 0 and become negative at the end of the simulations. The decreased CPD indicates more reduction of the right-handed polarized waves than the left-handed polarized ones by electrons via wave–electron cyclotron resonance interactions.

Over the whole time–frequency domain and for all electromagnetic waves in the simulation domain, energy anisotropies of their LPTE and RPTE (panel (g)) and the anisotropy of their CPDs (panel (h)) are also presented in Figure 7. Consistent with panels (e) and (f), RPTE predominates the total energy of transverse electric fields along most of the wave propagation directions in each $n_{\rm rb}/n_t$ case. Correspondingly, the CPDs at different wave propagation angles are, hence, mostly positive (right-handed polarized). Small negative (or left-handed polarized) CPDs, however, also exist for the $n_{\rm rb}/n_t = 30\%$ and 40% cases, e.g., along $\theta \geqslant 160°$. Furthermore, consistent with the classical definition of the perpendicular-propagating electromagnetic waves, their CPDs are always around 0 (linearly polarized) at $\theta = 90°$ for all cases. For parallel-propagating electromagnetic waves ($\theta = 0°$) in $n_{\rm rb}/n_t = 5\%$ and 10% cases, the resulting CPDs can reach 1.0, i.e., fully right-handed circularly polarized (see panels (a) and (b) of Figure 7 for $n_{\rm rb}/n_t = 5\%$). There the left-handed polarized O mode has negligible contributions to the total energies of the parallel-propagating electromagnetic waves.

All electromagnetic waves in the simulation domain are included in the above discussions. From the observational point of view, however, not all excited waves can be detected remotely. It is known that an electromagnetic wave can escape from an astrophysical plasma only if its refractive index is less than unity, i.e., $|ck/\omega| < 1$, and its frequency is larger than the local plasma frequency, i.e., $\omega > \omega_{\rm pe}$ (Melrose 1986; Budden 1988; Stix 1992; Benz 2002; Bellan 2006). Escaping electromagnetic waves in plasmas, hence, are only the O and X modes. Properties of the polarization and spectrogram are, hence, investigated for these escaping electromagnetic waves with $\omega > \omega_{\rm pe}$ and $|ck/\omega| < 1$ (the escape condition), shown in Figures 8 and 9, respectively. Other waves, with larger refractive indices and low frequencies, are trapped and can be absorbed or reflected (depending on their cutoff or/and resonance frequencies) during wave propagations in the IPM or interestellar plasmas. The only way that those waves can be remotely detected is by means of conversion to escaping electromagnetic waves via mechanisms such as wave–wave coupling, coalescence or decay, antenna mechanisms, or mode conversation in inhomogeneous plasmas (see, e.g., Graham et al. 2017, 2018, and references therein), which is, however, beyond the scope of this study.

Due to the removal of electromagnetic waves with $\omega \leqslant \omega_{\rm pe}$ or $|ck/\omega| \geqslant 1$ (mostly the whistler and Z modes), energies of both the escaping RPTE and LPTE are reduced (Figure 8(e)) in comparison with those of all electromagnetic waves in the simulation domain (Figure 7(e)). Another obvious difference between the escaping RPTE, LPTE and the RPTE, LPTE of all electromagnetic waves is that, when $n_{\rm rb}/n_t \leqslant 10\%$, the first growth phase (during $\omega_{\rm norm}\, t < 325$, which is associated with the beam instability) in the energy evolution profiles of the RPTE and LPTE of all electromagnetic waves does not exist anymore in Figure 8(e) for the escaping electromagnetic waves. That indicates that the excitations of the high-frequency escaping electromagnetic waves are mainly due to the ECM instability in plasmas with tenuous ring-beam electrons ($n_{\rm rb}/n_t \leqslant 10\%$), and the significant growth of the O mode associated with the beam instability in Figure 5(d) is likely caused by contamination from the Z mode in these tenuous ring-beam cases.

Figure 8(f) shows the evolution of the CPD for the escaping electromagnetic waves. In the cases with larger $n_{\rm rb}/n_t \geqslant 20\%$, one can see that the CPDs of the escaping electromagnetic

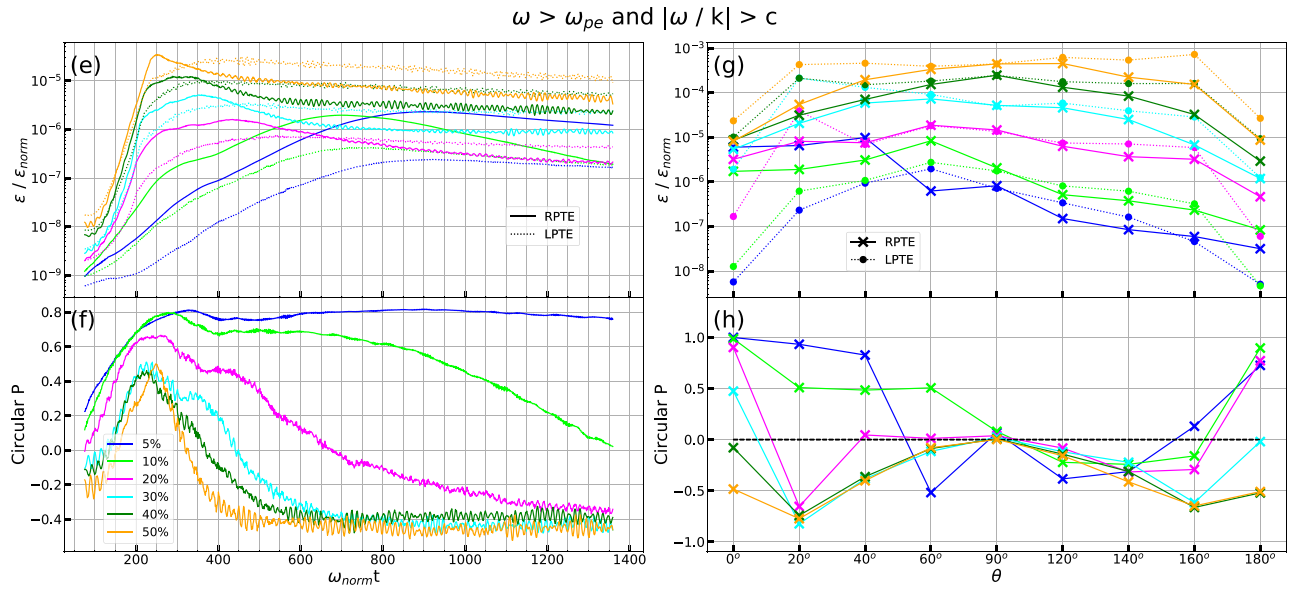

Figure 8. Same as panels (e) to (h) in Figure 7, but for transverse electric fields of the escaping electromagnetic waves with $\omega > \omega_{pe}$ and $|\omega/k| > c$.

waves are always smaller than those of all electromagnetic waves and can flip sign and be close to -0.4 at the end of simulations. In contrast, the CPDs of the escaping electromagnetic waves in $n_{rb}/n_t \leqslant 10\%$ cases are larger than those of all electromagnetic waves, especially around the saturation of the first growth phase in the energy evolution profile for all waves ($\sim\omega_{norm}\, t < 325$ in Figure 7(e)).

Figure 8(g) shows the energy anisotropies of the LPTE and RPTE for the escaping electromagnetic waves. Different from those of all the electromagnetic waves in the simulation domain, dominance of the RPTE or LPTE changes with the wave propagation direction θ in plasmas with tenuous ring-beam electrons $n_{rb}/n_t \geqslant 10\%$. For plasmas with dense ring-beam electrons (especially $n_{rb}/n_t \geqslant 30\%$), LPTE dominates the escaping transverse electric field energy along most of the wave propagation directions. Correspondingly, the anisotropy of the CPD for the escaping electromagnetic waves (Figure 8(h)) is also quite different from the one for all electromagnetic waves in the simulation domain (Figure 7(h)). For the escaping electromagnetic waves, a left-handed CPD can be found at some directions for each n_{rb}/n_t case. Furthermore, the left-handed CPD dominates over all wave propagation directions in plasmas with dense ring-beam electrons $n_{rb}/n_t \geqslant 40\%$. At $\theta = 90^\circ$, escaping electromagnetic waves are still linearly polarized. Additionally, with the increase of n_{rb}/n_t, the CPDs of the escaping electromagnetic waves become increasingly symmetric around $\theta = 90^\circ$, corresponding to their symmetric energies of the RPTE and LPTE (Figure 8(g)).

Figure 9 shows the dependences of the spectrograms of the RPTE and LPTE in escaping electromagnetic waves on the wave propagation direction. These spectrograms have similar anisotropy and symmetry properties (i.e., corresponds well) to their corresponding CPDs in Figure 8(h). With the exception of waves propagating near $\theta = 90^\circ$, the spectrograms of the RPTE and LPTE are quite different along any other propagation directions. These differences increase with increasing value of $|\theta - 90^\circ|$. And with Figure 9, one can also find that the CPD of these escaping electromagnetic waves depends not only on the wave propagation direction and the population of the ring-beam electrons, but also on the wave frequency and time. Furthermore, intense emissions in these spectrograms are generally located around the frequencies ω_{pe} and/or ω_{ce}. Bandwidths and intensities, as well as the patterns of these intense emissions, vary a lot among different frequencies, wave propagation directions, and populations of the ring-beam electrons. Emission around $2\omega_{ce}$ can also be found in these spectrograms, especially for the perpendicular propagation $\theta = 90^\circ$ and for plasmas with a dense ring-beam electron population.

3.2. ω_{ce}/ω_{pe} Dependence

As mentioned in Section 1, $\omega_{ce} > \omega_{pe}$ is required for an efficient escaping ECM emission. Many previous numerical studies for the ECM emission (e.g., Pritchett 1984; Lee et al. 2009, 2011), hence, considered situations with $\omega_{ce} > \omega_{pe}$. Although $\omega_{ce} > \omega_{pe}$ can exist in some density cavities owing to, e.g., turbulent magnetic field fluctuations (Wu et al. 2014; Chen et al. 2017; Melrose 2017), based on the standard solar atmosphere model (Wild 1985), $\omega_{ce} < \omega_{pe}$ is typical for the solar coronal conditions. In this section, we will focus on the wave excitation dependence on the ω_{ce}/ω_{pe} for ring-beam energetic electrons with fixed number density ratio n_{rb}/n_t to 5% and fixed total electron plasma frequency ω_{pe}. This is justified considering that the typical gradient length of the particle number density is usually larger than that of the magnetic field strength in the solar corona (see Equations (1.6.1) and (1.4.2) in Aschwanden 2005). The ratio between the electron cyclotron frequency ω_{ce} and ω_{pe} takes 0.2, 0.3, 0.5, 1, 2, and 3, while the case $\omega_{ce}/\omega_{pe} = 5$ has been analyzed in Section 3.1. Similar to Figure 4, the dispersion spectrum dependences on the ω_{ce}/ω_{pe} and wave propagation direction θ are presented in Figure 10.

As for the case with $\omega_{ce}/\omega_{pe} = 5$, excitations of the beam, Langmuir (row (a)), whistler (row (b)), O (row (c)), Z (row (d)), and X (row (e)) modes still exist in each $\omega_{ce}/\omega_{pe} < 5$ case. Intensities of the escaping electromagnetic waves from the weakly magnetized plasmas $\omega_{ce}/\omega_{pe} < 1$ are, however, significantly suppressed and negligible compared with those from plasmas with $\omega_{ce}/\omega_{pe} > 1$, which is consistent with the statement of Vlahos (1987). With the decrease of the

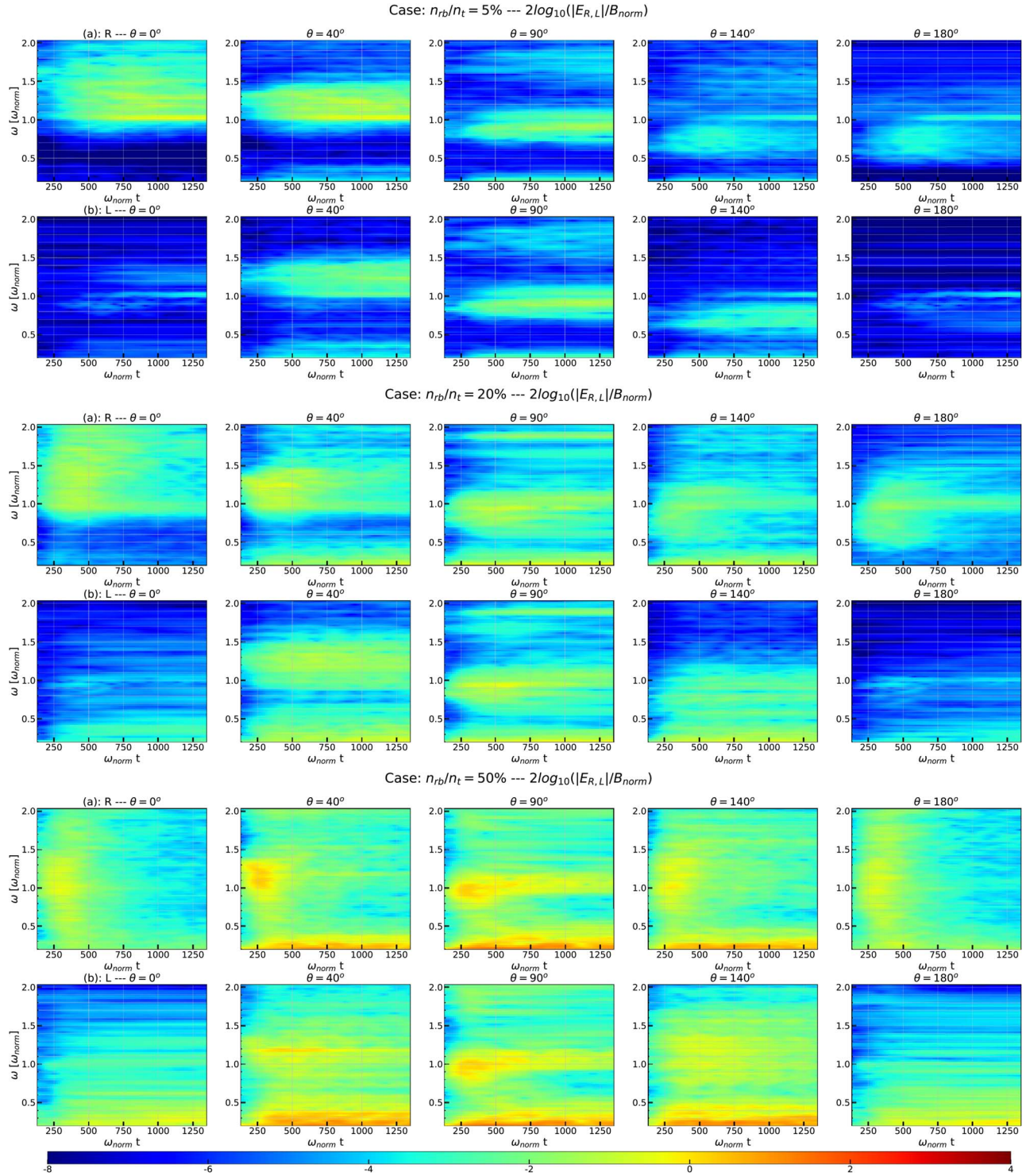

Figure 9. Spectrograms of the RPTE and LPTE in escaping electromagnetic waves (with $\omega > \omega_{pe}$ and $|ck/\omega| < 1$) along different wave propagation directions θ (=0°, 40°, 90°, 140° and 180° from the left to right column, respectively) for plasmas with $n_{rb}/n_t = 5\%$ (top two rows), 20% (middle two rows), and 50% (bottom two rows) and $\omega_{ce}/\omega_{pe} = 5.0$. In each n_{rb}/n_t case, rows (a) and (b) are for the RPTE and LPTE, respectively. All panels use the same color bar shown at the bottom.

ω_{ce}/ω_{pe}, the dispersion relation surfaces of the O and X modes tend to overlap with each other in the cold-plasma approximation. The intensity differences between the O and X modes, hence, cannot be well resolved for small ω_{ce}/ω_{pe} cases with the limited resolution in the ω space in our simulations. Quantitative investigations of the energy and polarization property dependences on the ω_{ce}/ω_{pe} ratio will be presented in following papers with a higher ω resolution. Here we will concentrate on discussing the harmonic excitations of the ω_{pe} and ω_{ce}.

In Figure 10, one can find that excitations at higher and higher harmonics s_h of both ω_{pe} (rows (a) and (b)) and ω_{ce} (rows (c) to (e)) appear with the decrease of the ω_{ce}/ω_{pe}. However, excitations of ω_{pe} harmonics can only be found in cases with $\omega_{ce}/\omega_{pe} < 1$, i.e., weakly magnetized plasmas. In row (b), although frequencies of the excited harmonics of ω_{pe}

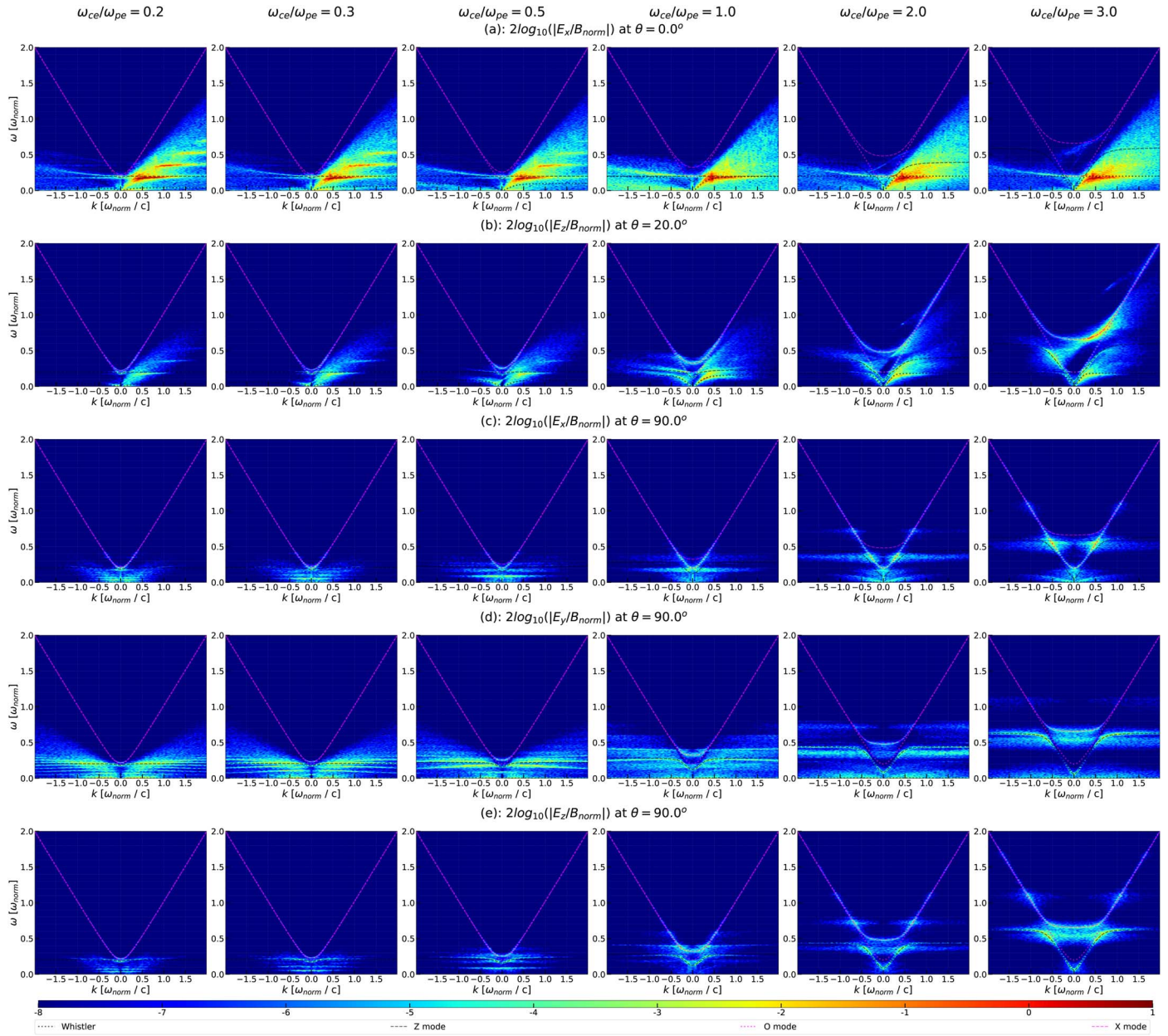

Figure 10. Similar to Figure 4, but for plasmas with $n_{rb}/n_t = 5\%$ but different ω_{ce}/ω_{pe}, from the left to right columns, $\omega_{ce}/\omega_{pe} = 0.2$, 0.3, 0.5, 1, 2, 3, respectively. Row (a) is for E_x with $\theta = 0°$. Row (b) is for E_z with $\theta = 20°$. Row (c) is for E_x with $\theta = 90°$. Row (d) is for E_y with $\theta = 90°$. Row (e) is for E_z with $\theta = 90°$. Also note that the color scale in this figure is, however, different from that in Figure 4.

are evidently higher than ω_{pe}, the refractive indices in these harmonics of ω_{pe} are, however, much larger than 1. These waves are likely reflected at the boundary of plasmas with distinct properties, and they therefore cannot be observed remotely. Meanwhile, these non-escaping harmonics of ω_{pe} are mainly located in the direction quasi-parallel to the ambient magnetic field $\boldsymbol{B}_0$, implying a beam instability origin. Note that these excited non-escaping harmonics of ω_{pe} are not centered exactly at the integer multiples of ω_{pe}. Instead, their frequencies increase with k, i.e., with a small positive slope in each non-escaping harmonic ω_{pe} band. Similar results can also be found in the study of Thurgood & Tsiklauri (2015) for the plasma emission theory. These frequency shifts in the fundamental ω_{pe} mode have been attributed to deviations from the prediction of the cold-plasma theory in the case of dense beams (Fuselier et al. 1985; Cairns 1989), where the beam-mode waves might affect the generation of the fundamental ω_{pe} mode. And the frequency shifts at higher non-escaping harmonics of ω_{pe} are, perhaps, due to the frequency shift of the fundamental ω_{pe} mode, since the fundamental mode is responsible for the excitations of other higher harmonics. Enhanced harmonics of ω_{ce} can be found in each panel of rows (c) to (e) of Figure 10. In other words, excitation of harmonic ω_{ce} does not depend on the magnetized condition of plasma ω_{ce}/ω_{pe}. Additionally, these excited harmonics of ω_{ce} are likely excited by the ECM instability, since excitation of them is mainly located in the direction perpendicular to the ambient magnetic field $\boldsymbol{B}_0$.

Although the excitation mechanisms for the harmonics of ω_{pe} and ω_{ce} are totally different, they still have some common characteristics. For instance, all these harmonic waves contain both longitudinal (row (a) for s_h ω_{pe}, row (d) for s_h ω_{ce}) and transverse (row (b) for s_h ω_{pe}, rows (c) and (e) for s_h ω_{ce})

components, but the longitudinal component is stronger than the transverse one, which is opposite to those of the Z and X modes in the perpendicular direction. Harmonic excitation of ω_{pe} with a preferential longitudinal component has been found previously by Klimas (1983), Nishikawa & Cairns (1991), Yoon et al. (2003), Yi et al. (2007), and Rhee et al. (2009). Additionally, intensities in these excited harmonics of ω_{pe} and ω_{ce} decrease with the increase of the harmonic number. Moreover, all excited harmonics of ω_{pe} and ω_{ce} are non-escaping modes in weakly magnetized plasmas with $\omega_{ce}/\omega_{pe} < 1$.

4. Conclusions and Discussion

Using 2.5D fully kinetic PIC simulations, we investigated the energy and polarization properties of electromagnetic waves excited by mildly relativistic ring-beam electrons in neutral and current-free solar coronal plasmas. These energetic ring-beam electrons could be produced by magnetic reconnection, quasi-perpendicular shocks, and/or electron beams propagating in inhomogeneous magnetic fields in the solar corona. These ring-beam electrons, together with the background electrons and protons, support the global current and charge neutralities in these plasmas, where all background electrons drift oppositely to the ring-beam electrons (i.e., return current) to fully compensate the current induced by the ring-beam electrons, i.e., a neutral ring-beam-return current system. To apply the simulation results to solar radio observations and considering variations of the electron ring-beam density and magnetic field strength along the path of electron propagation, we explore the dependences of the electromagnetic wave excitations on the number density ratio of the ring-beam electrons over the total electrons (n_{rb}/n_t) and the ratio of the electron cyclotron frequency (ω_{ce}) to the electron plasma frequency (ω_{pe}).

We found that the beam and ECM instabilities together can efficiently excite the whistler-, Z-, O-, and X-mode electromagnetic waves, as well as harmonics of ω_{pe} (only when $\omega_{ce}/\omega_{pe} < 1$) and ω_{ce}. We also found the excitations of electrostatic waves, relativistic Bernstein waves, and some diffusive nonlinear waves that do not follow well-defined dispersion relations. Electrostatic waves always dominate the energetics of all excited waves. These electrostatic waves can lead to significant heatings on the ring-beam and background electrons due to Landau damping.

Properties of the electromagnetic whistler-, Z-, O-, and X-mode waves were studied in detail. In order to obtain the energy evolutions of these electromagnetic waves, we adopted a Gaussian filter centered on the wave dispersion surfaces of the magnetized cold plasmas in the wavevector–frequency ($\boldsymbol{k} - \omega$) space and assumed a frequency broadening of all excited electromagnetic waves $\sigma = 0.05\omega_{norm}$, which is frequently seen in the spectrograms of escaping electromagnetic waves (Figure 9). For a convergence test, we also carried calculations with $\sigma = 0.03\omega_{norm}$ and $0.2\omega_{norm}$, while the frequency resolution in our PIC simulations is $3 \times 10^{-3}\omega_{norm}$. We found that results with $\sigma = 0.03\omega_{norm}$ and $0.05\omega_{norm}$ are almost the same. We admit that this Gaussian filter method for energy of a wave mode might contain contamination from other waves particularly when the dispersion relations of two wave modes are close to each other. Additionally we might also underestimate the energies of diffusive waves with a fixed σ for all wave modes. However, in general, this method gives more accurate information about the mode energy compared to estimates given in the previous studies (see, e.g., Pritchett 1984; Lee et al. 2009, 2011).

Based on the Gaussian filter method, we carried out detailed studies of the dependences of the excited electromagnetic whistler-, Z-, O-, and X-mode properties on the ring-beam electron density for $\omega_{ce}/\omega_{pe} = 5$ and found the following:

1. Both the beam and ECM instabilities contribute to the excitation of these electromagnetic waves. The beam instability dominates the saturations of the whistler and Z modes, as well as O mode in plasmas with dense ring-beam electrons. But the X-mode waves cannot be efficiently excited by the beam instability only, especially with tenuous ring-beam electrons.
2. In the growth phase of a wave mode, the free energy dissipation rate and the wave growth rate, in general, increase with the increase of the ring-beam density. The growth rates of the whistler and Z modes are comparable but higher than those of the O and X modes.
3. The saturation levels of different electromagnetic wave modes also increase with the increase of n_{rb}/n_t, except for the X-mode waves produced by low-density ring-beam electrons. The X-mode saturation level for $n_{rb}/n_t = 5\%$ is actually higher than that for $n_{rb}/n_t = 10\%$.
4. The energy of each electromagnetic wave mode is strongly anisotropic. This anisotropy is suppressed in plasmas with dense ring-beam electrons, where the X mode has the strongest anisotropy.

Although only the O and X modes are remotely detectable and related more to the remote observations of the SRBs, the individual investigation of the energy properties of all the whistler, Z, O, and X modes obtained here will complement their linear and quasi-linear theoretical studies. In theoretical studies, nonlinear processes (e.g., wave–wave and wave–particle cyclotron resonance interactions) and evolution of the plasma system itself (e.g., population of the energetic and background electrons, plasma temperature) cannot be usually treated self-consistently. In this study, we found that all these processes affect the energy saturations and growth rates of those wave modes.

Harmonic excitations of ω_{pe} and ω_{ce} are studied for differently magnetized plasmas with $0.2 \leqslant \omega_{ce}/\omega_{pe} \leqslant 5$. Over all simulated cases, one can find that harmonics of ω_{ce} can be always excited, while there is no obvious excitation for the escaping harmonics of ω_{pe}. Such results were also found by Ganse et al. (2012b). As mentioned by Thurgood & Tsiklauri (2015), as well as according to Equation (6.80) in Melrose (1986) for the probability of the $L + L' \rightarrow T_{2\omega_{pe}}$ process, the key reason for the absence of the escaping harmonics of ω_{pe} in our simulated plasmas could be the weak intensities (in plasmas with tenuous ring-beam electrons $n_{rb}/n_t \leqslant 20\%$) and/or the predominant wave intensities located at small wavenumber $|k|$ (due to Landau damping in plasmas with dense ring-beam electrons) of both the parallel- and antiparallel-propagating electrostatic Langmuir waves. Based on the study of Thurgood & Tsiklauri (2015), escaping harmonics of ω_{pe} are more likely present in plasmas with very tenuous beam electrons $n_{rb}/n_t < 0.6\%$, and generations of the harmonics of ω_{pe} are very sensitive to the chosen parameters, like the populations of the beam and oppositely drifting electrons, the drifting velocity of the beam electrons, the magnetized condition, etc.

(Rhee et al. 2009; Umeda 2010; Ganse et al. 2012b; Thurgood & Tsiklauri 2015; Henri et al. 2019). The setup parameters used here, however, favor more the excitation of the beam mode instead of Langmuir waves.

Non-escaping harmonics of ω_{pe} can be excited only when $\omega_{ce}/\omega_{pe} < 1$. Higher and higher non-escaping harmonics of ω_{pe} are driven with the decrease of ω_{ce}/ω_{pe}. No matter whether escaping harmonics of ω_{pe} are excited or not, the beam instability can always lead to the excitations of the Langmuir, whistler-, Z-, and O-mode waves. ECM excitations of the harmonics of ω_{ce}, however, do not depend on the ratio of ω_{ce}/ω_{pe}. In other words, $s_h\ \omega_{ce}$ (as well as X mode) will be excited as long as the free energy $\partial f/\partial u_\perp > 0$ exists for the ECM instability. The requirement of $\omega_{ce}/\omega_{pe} > 1$ in the ECM emission theory is for an efficient generation of observable escaping emissions by remote detections, i.e., the escape condition (see Section 1).

In addition, to compare with solar radio observations, we also obtained the polarization properties (CPD, spectrogram) of the electromagnetic waves, in particular of the escaping electromagnetic waves with $\omega > \omega_{pe}$ and $|ck/\omega| < 1$. In summary, escaping emission decreases rapidly with the decrease of ω_{ce}/ω_{pe}. In weakly magnetized plasmas with $\omega_{ce}/\omega_{pe} < 1$, most of the excited escaping electromagnetic waves are located close to the plasma frequency ω_{pe}, and their energies are significantly weaker and negligible compared to those of plasmas with $\omega_{ce}/\omega_{pe} > 1$, i.e., strongly magnetized plasmas. Energy and polarization properties of the escaping electromagnetic waves in strongly magnetized plasmas depend on the density ratio n_{rb}/n_t:

1. When $n_{rb}/n_t \leqslant 10\%$, the ECM instability dominates the excitations of the escaping electromagnetic waves. RPTEs dominate the transverse electric field energies of the escaping electromagnetic waves. And right-handed polarized CPDs can be expected along many wave propagation directions. Moreover, the strongest escaping emission is in the same side of the ring-beam electron propagation direction (i.e., $\theta < 90°$). These properties may explain observed properties of solar radio spikes.
2. For plasmas with dense ring-beam electrons $n_{rb}/n_t \geqslant 20\%$, the escaping emissions are dominated by the ECM instability at the beginning. The beam instability plays a more important role later on, giving rise to more isotropic and LPTE-dominated emissions, which may be applied to observations of type III bursts.

Considering the population reduction of the ring-beam electrons during their propagations in the solar corona, these results might explain the increased time delay of the type III bursts (<1 s) and solar radio spikes (2–5 s) to the hard X-ray bursts (see Fleishman & Mel'nikov 1998 for a review of the solar radio spikes). Moreover, diversities in the SRBs' CPD and spectrogram observations may already originate from their generation sites.

Our results above deal with properties of waves driven by energetic ring-beam electrons at the site of wave generation, where the global charge and current neutralities are maintained via protons and drifting background electrons, respectively. Note that the remotely observed energy and polarization properties of the SRBs might deviate from those in their source regions, due to some propagation effects of the electromagnetic waves (e.g., reflection, refraction, Faraday rotation, energy absorption via wave–particle interaction) along the wave path in the IPM. For an accurate prediction of the remote SRB observations, one, hence, still needs to combine our simulations with a proper model describing the wave propagation effects in the IPM (Li et al. 2008a, 2008b, 2009). This study is, however, still meaningful to gain insight into the generation mechanisms of the original coherent emission by energetic ring-beam electrons in the neutral and current-free solar coronal plasmas, where all background electrons drift oppositely to the ring-beam electrons to fully compensate the current induced by the ring-beam electrons.

Finally, we note that dynamic processes in plasmas with energetic ring-beam electrons contain not only the excitations of waves but also plasma heating and electron acceleration. Significant plasma heating and electron acceleration can be expected, particularly, in plasmas with dense ring-beam electrons, where a significant fraction of the ring-beam electrons can be reflected, making the system more or less symmetric with respect to the plane perpendicular to the ambient magnetic field $\boldsymbol{B}_0$. Due to the acceleration of electrons, a double power-law distribution is formed in the high-energy tail ($\gamma - 1 > 0.1 \sim 50$ keV) of the electron energy distribution when the wave–particle plasma system reaches an equilibrium.

We gratefully acknowledge the developers of the ACRONYM code, the Verein zur Förderung kinetischer Plasmasimulationen e.V. In particular, we thank Patrick Kilian for helpful discussions and valuable suggestions. X.Z. thanks the International Partnership Program of Chinese Academy of Sciences (No. 114332KYSB20170008) and the International Cooperation and Exchange Project of National Natural Science Foundation of China (No. 11761131007) for support. P.A.M. acknowledges his financial support by the German Science Foundation DFG, project MU-4255/1-1. We also acknowledge the computing resources in the Max Planck Computing and Data Facility (MPCDF, formerly known as RZG) at Garching, Germany, and the Max Planck Institute for Solar System Research, Germany.

ORCID iDs

Xiaowei Zhou https://orcid.org/0000-0001-7855-2479
Patricio A. Muñoz https://orcid.org/0000-0002-3678-8173
Jörg Büchner https://orcid.org/0000-0002-5700-987X
Siming Liu https://orcid.org/0000-0003-1039-9521

References

Alvarez, H., & Haddock, F. T. 1973, SoPh, 29, 197
Andre, M. 1985, JPlPh, 33, 1
Aschwanden, M. J. 2002, SSRv, 101, 1
Aschwanden, M. J. 2005, Physics of the Solar Corona. An Introduction with Problems and Solutions (2nd ed.; Chichester: Praxis Publishing Ltd.)
Bellan, P. M. 2006, Fundamentals of Plasma Physics (Cambridge: Cambridge Univ. Press)
Benz, A. (ed.) 2002, Plasma Astrophysics (2nd ed.; Dordrecht: Kluwer)
Benz, A. O. 1985, SoPh, 96, 357
Benz, A. O. 1994, SSRv, 68, 135
Benz, A. O. 2008, LRSP, 5, 1
Bessho, N., Chen, L. J., Shuster, J. R., & Wang, S. 2014, GeoRL, 41, 8688
Birdsall, C. K., & Langdon, A. B. 1991, Plasma Physics via Computer Simulation (Bristol: Adam Hilger Ltd.)
Bittencourt, J. A. 2004, Fundamentals of Plasma Physics (Berlin: Springer)
Brown, J. C., & Bingham, R. 1984, A&A, 131, L11

Büchner, J., Kilian, P., Muñoz, P. A., et al. 2018, in Magnetic Fields in the Solar System: Planets, Moons and Solar Wind Interactions, ed. H. Lühr et al. (Cham: Springer), 201
Büchner, J., & Kuska, J.-P. 1996, JGG, 48, 781
Budden, K. G. 1988, The Propagation of Radio Waves (Cambridge: Cambridge Univ. Press)
Cairns, I. H. 1989, PhFlB, 1, 204
Cairns, I. H., Lobzin, V. V., Donea, A., et al. 2018, NatSR, 8, 1676
Carozzi, T. D., Thidé, B., Leyser, T. B., et al. 2001, JGR, 106, 21395
Chen, B., Bastian, T. S., Shen, C., et al. 2015, Sci, 350, 1238
Chen, B., Yu, S., Battaglia, M., et al. 2018, ApJ, 866, 62
Chen, L., Thorne, R. M., Shprits, Y., & Ni, B. 2013, JGRA, 118, 2185
Chen, L., Wu, D. J., Zhao, G. Q., & Tang, J. F. 2017, JGRA, 122, 35
Comişel, H., Verscharen, D., Narita, Y., & Motschmann, U. 2013, PhPl, 20, 090701
Dawson, J. M. 1983, RvMP, 55, 403
De Groot, T. 1962, Int. Bull. Solar Radio Obs. Europe, 9, 3
Drake, J. F., Swisdak, M., Cattell, C., et al. 2003, Sci, 299, 873
Droege, F., & Riemann, P. 1961, Int. Bull. Solar Radio Obs. Europe, 8, 6
Dulk, G. A. 1985, ARA&A, 23, 169
Elgarøy, Ø. 1961, ApNr, 7, 123
Ergun, R. E., Larson, D., Lin, R. P., et al. 1998, ApJ, 503, 435
Fleishman, G. D., & Mel'nikov, V. F. 1998, PhyU, 41, 1157
Fletcher, L., & Hudson, H. S. 2008, ApJ, 675, 1645
Freund, H. P., Wong, H. K., Wu, C. S., & Xu, M. J. 1983, PhFl, 26, 2263
Fuselier, S. A., Gurnett, D. A., & Fitzenreiter, R. J. 1985, JGR, 90, 3935
Ganse, U., Kilian, P., Spanier, F., & Vainio, R. 2012a, ApJ, 751, 145
Ganse, U., Kilian, P., Vainio, R., & Spanier, F. 2012b, SoPh, 280, 551
Gaponov, A. 1959, IzVUZ, 2, 450
Gary, S. P. 1993, Theory of Space Plasma Microinstabilities (Cambridge: Cambridge Univ. Press)
Ginzburg, V. L., & Zhelezniakov, V. V. 1958, SvA, 2, 653
Goldreich, P., & Julian, W. H. 1969, ApJ, 157, 869
Graham, D. B., Khotyaintsev, Y. V., Vaivads, A., et al. 2017, PhRvL, 119, 025101
Graham, D. B., Vaivads, A., Khotyaintsev, Y. V., et al. 2018, JGRA, 123, 2630
Henri, P., Sgattoni, A., Briand, C., Amiranoff, F., & Riconda, C. 2019, JGRA, 124, 1475
Hockney, R. W. 1971, JCoPh, 8, 19
Kainer, S., & MacDowall, R. J. 1996, JGR, 101, 495
Karlický, M., & Bárta, M. 2009, NPGeo, 16, 525
Karlický, M., & Bárta, M. 2011, in IAU Symp. 274, Advances in Plasma Astrophysics, ed. A. Bonanno, E. de Gouveia Dal Pino, & A. G. Kosovichev (Cambridge: Cambridge Univ. Press), 252
Kempf, A., Kilian, P., & Spanier, F. 2016, A&A, 585, A132
Khodachenko, M. L., Zaitsev, V. V., Kislyakov, A. G., & Stepanov, A. V. 2009, SSRv, 149, 83
Kilian, P., Muñoz, P. A., Schreiner, C., & Spanier, F. 2017, JPlPh, 83, 707830101
Klimas, A. J. 1983, JGRA, 88, 9081
Landau, L. D. 1946, J. Phys. (USSR), 10, 25
Lapenta, G. 2012, JCoPh, 231, 795
Lee, K. H., Omura, Y., & Lee, L. C. 2011, PhPl, 18, 092110
Lee, K. H., Omura, Y., Lee, L. C., & Wu, C. S. 2009, PhRvL, 103, 105101
Lee, L. C., Kan, J. R., & Wu, C. S. 1980, P&SS, 28, 703
Lee, L. C., & Wu, C. S. 1980, PhFl, 23, 1348
Li, B., Cairns, I. H., & Robinson, P. A. 2008a, JGRA, 113, A06104
Li, B., Cairns, I. H., & Robinson, P. A. 2008b, JGRA, 113, A06105
Li, B., Cairns, I. H., & Robinson, P. A. 2009, JGRA, 114, A02104
Lin, R. P., Potter, D. W., Gurnett, D. A., & Scarf, F. L. 1981, ApJ, 251, 364
Matsumoto, H., & Omura, Y. 1993, Computer Space Plasma Physics: Simulation Techniques and Software (Tokyo: Terra Scientific Publishing Company), https://www.terrapub.co.jp/e-library/cspp/
McMaster, W. H. 1954, AmJPh, 22, 351
Melrose, D. B. 1973, AuJPh, 26, 229
Melrose, D. B. 1986, Instabilities in Space and Laboratory Plasmas (Cambridge: Cambridge Univ. Press)
Melrose, D. B. 1990, SoPh, 130, 3
Melrose, D. B. 1994, SSRv, 68, 159
Melrose, D. B. 2017, RvMPP, 1, 5
Melrose, D. B., & Wheatland, M. S. 2016, SoPh, 291, 3637
Morosan, D. E., Zucca, P., Bloomfield, D. S., & Gallagher, P. T. 2016, A&A, 589, L8
Muñoz, P. A., & Büchner, J. 2016, PhPl, 23, 102103
Muñoz, P. A., & Büchner, J. 2018a, ApJ, 864, 92
Muñoz, P. A., & Büchner, J. 2018b, PhRvE, 98, 043205
Nishikawa, K.-I., & Cairns, I. H. 1991, JGR, 96, 19343
Petrosian, V., & Liu, S. 2004, ApJ, 610, 550
Pritchett, P. L. 1984, JGR, 89, 8957
Pritchett, P. L., & Coroniti, F. V. 2004, JGRA, 109, A01220
Pritchett, P. L., Strangeway, R. J., Carlson, C. W., et al. 1999, JGR, 104, 10317
Régnier, S. 2015, A&A, 581, A9
Reid, H. A. S., & Ratcliffe, H. 2014, RAA, 14, 773
Rhee, T., Ryu, C.-M., Woo, M., et al. 2009, ApJ, 694, 618
Schneider, J. 1959, PhRvL, 2, 504
Schreiner, C., Kilian, P., & Spanier, F. 2017, ApJ, 834, 161
Shuster, J. R., Chen, L. J., Daughton, W. S., et al. 2014, GeoRL, 41, 5389
Shuster, J. R., Chen, L. J., Hesse, M., et al. 2015, GeoRL, 42, 2586
Stix, T. H. 1962, The Theory of Plasma Waves (New York: Mc-Graw Hill)
Stix, T. H. 1992, Waves in Plasmas (New York: AIP)
Strangeway, R. J., Ergun, R. E., Carlson, C. W., et al. 2001, PCEC, 26, 145
Stupp, A. 2000, MNRAS, 311, 251
Suzuki, S., & Dulk, G. A. 1985, in Bursts of Type III and Type V, ed. D. J. McLean & N. R. Labrum (Cambridge: Cambridge Univ. Press), 289
Thurgood, J. O., & Tsiklauri, D. 2015, A&A, 584, A83
Treumann, R. A., & Baumjohann, W. 2017, AnGeo, 35, 999
Treumann, R. A., Baumjohann, W., & Pottelette, R. 2011, AnGeo, 29, 1885
Treumann, R. A., Baumjohann, W., & Pottelette, R. 2012, AnGeo, 30, 119
Tsang, K. T. 1984, PhFl, 27, 1659
Tskhakaya, D., Matyash, K., Schneider, R., & Taccogna, F. 2007, CoPP, 47, 563
Tsurutani, B. T., & Lakhina, G. S. 1997, RvGeo, 35, 491
Twiss, R. Q. 1958, AuJPh, 11, 564
Umeda, T. 2010, JGRA, 115, A01204
Umeda, T., Ashour-Abdalla, M., Schriver, D., Richard, R. L., & Coroniti, F. V. 2007, JGRA, 112, A04212
Vandas, M., & Hellinger, P. 2015, PhPl, 22, 062107
van den Oord, G. H. J. 1990, A&A, 234, 496
Vay, J.-L., & Godfrey, B. B. 2014, CRMec, 342, 610
Vlahos, L. 1987, SoPh, 111, 155
Vlahos, L., & Cargill, P. 2009, Turbulence in Space Plasmas (Berlin: Springer)
Vlahos, L., & Sprangle, P. 1987, ApJ, 322, 463
Voitcu, G., & Echim, M. 2018, AnGeo, 36, 1521
Voitcu, G., & Echim, M. M. 2012, PhPl, 19, 022903
Wild, J. P. 1985, in The Beginnings (of Solar Radiophysics), ed. D. J. McLean & N. R. Labrum (Cambridge: Cambridge Univ. Press), 3
Wild, J. P., Sheridan, K. V., & Neylan, A. A. 1959, AuJPh, 12, 369
Wild, J. P., Smerd, S. F., & Weiss, A. A. 1963, ARA&A, 1, 291
Willes, A. J., & Cairns, I. H. 2000, PhPl, 7, 3167
Wu, C. 2012, ChSBu, 57, 1357
Wu, C. S., & Freund, H. P. 1984, RaSc, 19, 519
Wu, C. S., & Lee, L. C. 1979, ApJ, 230, 621
Wu, D. J. 2014, PhPl, 21, 064506
Wu, D. J., Chen, L., Zhao, G. Q., & Tang, J. F. 2014, A&A, 566, A138
Yi, S., Yoon, P. H., & Ryu, C.-M. 2007, PhPl, 14, 013301
Yoon, P. H., Gaelzer, R., Umeda, T., Omura, Y., & Matsumoto, H. 2003, PhPl, 10, 364
Zhou, X., Büchner, J., Bárta, M., Gan, W., & Liu, S. 2015, ApJ, 815, 6
Zhou, X., Büchner, J., Bárta, M., Gan, W., & Liu, S. 2016, ApJ, 827, 94